arXiv:1610.08079v2 [cond-mat.str-el] 15 Dec 2016

Origin of Kinks in Energy Dispersion of Strongly Correlated Matter

Kazue Matsuyama[1], Edward Perepelitsky[2,3] and B Sriram Shastry[1]

[1] *Physics Department, University of California, Santa Cruz, CA 95064*

[2] *Centre de Physique Théorique, École Polytechnique, CNRS, Université Paris-Saclay, 91128 Palaiseau, France*

[3] *Collège de France, 11 place Marcelin Berthelot, 75005 Paris, France*

(Dated: December 19, 2016)

Abstract

We investigate the origin of ubiquitous low energy kinks found in Angle Resolved Photoemission (ARPES) experiments in a variety of correlated matter. Such kinks are unexpected from weakly interacting electrons and hence identifying their origin should lead to fundamental insights in strongly correlated matter. We devise a protocol for extracting the kink momentum and energy from the experimental data which relies solely on the two asymptotic tangents of each dispersion curve, away from the feature itself. It is thereby insensitive to the different shapes of the kinks as seen in experiments. The body of available data is then analyzed using this method. We proceed to discuss two alternate theoretical explanations of the origin of the kinks. Some theoretical proposals invoke local Bosonic excitations (Einstein phonons or other modes with spin or charge character), located exactly at the energy of observed kinks, leading to a *momentum independent* self energy of the electrons. A recent alternate is the theory of extremely correlated Fermi liquids (ECFL). This theory predicts kinks in the dispersion arising from a *momentum dependent* self energy of correlated electrons. We present the essential results from both classes of theories, and identify experimental features that can help distinguish between the two mechanisms. The ECFL theory is found to be consistent with currently available data on kinks in the nodal direction of cuprate superconductors, but conclusive tests require higher resolution energy distribution curve data.

INTRODUCTION

High precision measurements of electronic spectral dispersions has been possible in recent years, thanks to the impressive enhancement of the experimental resolution in the angle resolved photoemission spectroscopy (ARPES). This technique measures the single electron spectral function $A(\vec{k},\omega)$ multiplied by the Fermi occupation function; it can be scanned at either fixed $\vec{k}$ as a function of ω or at fixed ω as a function of $\vec{k}$. These scans produce respectively the energy distribution curves (EDCs) and momentum distribution curves (MDCs). The line shapes in both these scans are of fundamental interest, since they provide a direct picture of the quasiparticle and background components of interacting Fermi systems, and thus unravel the roles of various interactions that are at play in strongly correlated Fermi systems. The dispersion relation of the electrons can be studied through the location of the peaks of $A(\vec{k},\omega)$ in constant ω or constant $\vec{k}$ scans.

Recent experimental studies have displayed a surprising ubiquity of *kinks* in the dispersion of strongly correlated matter at low energies $\sim 50-100$ meV. The kinks are bending type anomalies (see Fig. (1)) of the simple $\omega = v_F(\vec{k}-\vec{k}_F)$, i.e. linear energy versus momentum dispersion that is expected near $\vec{k}_F$ from band theory. The special significance of kinks lies in the fact that their existence *must* signal a *departure* from band theory. This departure could be either due to electron-electron interactions, or to interaction of the electrons with other Bosonic degrees of freedom. Either of them are therefore significant enough to leave a direct and observable fingerprint in the spectrum. The goal of this work is to elucidate the origin of the observed kinks, and therefore to throw light on the dominant interactions that might presumably lead to high Tc superconductivity.

The purpose of this paper is multifold, we (i) survey the occurrence of the kinks in a variety of correlated systems of current interest, (ii) provide a robust protocol for characterizing the kinks which is insensitive to the detailed shape of the kink, (iii) discuss how these kinks arise in two classes of theories, one based on coupling to a Bosonic mode and the other to strong correlations, and (iv) identify testable predictions that ARPES experiments can use to distinguish between these.

The fifteen systems reporting kinks are listed in Table (I); these include (1) most high T_c cuprates in the (nodal) direction $\langle 11\rangle$ at various levels of doping from insulating to normal metallic states in the phase diagram [1, 2] (2) charge density wave systems, (3) cobaltates

and (4) ferromagnetic iron surfaces. The kinks lose their sharpness as temperature is raised [2–4], and appear to evolve smoothly between the d-wave superconducting state and the normal state.

Name of the compounds					Local Bosonic Mode		
	Above Tc		Below Tc				
	MDC	EDC	MDC	EDC	Charge	Spin	Not reported
LSCO	✓[3, 13]		✓[1, 3, 13, 14]	✓[15]	✓[16–18]	✓[19]	
Bi2201	✓[3, 5, 13, 20, 21]	✓[22]	✓[5, 21]		✓[23]		
Bi2212	✓[2–5, 13, 24, 25]	✓[4]	✓[2–5, 13, 24, 25]		✓[26]	✓[27, 28]	
Bi2223	✓[5, 29]		✓[5, 29, 30]				✓
YBCO			✓[31]		✓[32, 33]	✓[34–37]	
Hg1201			✓[38]		✓[39]	✓[40–42]	
F0234			✓[43]				✓
CCOC			✓[44]				✓
LSMO			✓[45]	✓[45]			✓
2H-TaSe2 (CDW)			✓[46]		✓[47]		
Iron (110) surface			✓[48] 85 K				✓
BiBaCo1			✓[49] 5K	✓[49] 5K			✓
BiBaCo2			✓[49] 5K	✓[49] 5K			✓
BiBaCo	✓[49] 200K	✓[49] 200K					✓
NaCoO			✓[49] 5K	✓[49] 5K			✓

TABLE I: Comprehensive survey for ARPES kinks

The kinks above T_c are smoothed out as one moves away from nodal direction [5]. Recent experiments [6] resolve this movement of the kinks more finely into two sub features. Most of

the studies in Table (I) focus on MDC kinks, the EDC kinks data is available for only eight systems so far. Bosonic modes have been reported in six systems using different probes such as inelastic x-rays or magnetic scattering, with either charge (phonons, plasmons) or spin (magnetic) character, while the remaining nine systems do not report such modes. A few theoretical studies of the kinks have implicated the observed low energy modes via electron-Boson type calculations; we summarize this calculation in the Supplementary Information (SI) [7]. We find, in agreement with earlier studies, that the Boson coupling mechanism yields kinks in the MDC dispersion, provided the electron-Boson coupling is taken to be sufficiently large. In addition, we find in all cases studied, this mechanism also predicts a jump in the EDC dispersion. It also predicts an extra peak in the spectral function pinned to the kink energy after the wave vector crosses the kink. These two features are experimentally testable and differ from the predictions of the correlations mechanism discussed next.

Since kinks are also observed in cases where no obvious Bosonic mode is visible, it is important to explore alternate mechanisms that give rise to such features. In this context we note that a recent theoretical work using the extremely strongly correlated Fermi liquid (ECFL) theory [8, 9] calculates the dispersion using a low momentum and frequency expansions of the constituent self energies. This calculation [9] shows that both EDC and MDC energy dispersions display qualitatively similar kinks, in particular there is no jump in either dispersion. In essence this work implies that a purely electronic mechanism with a strong momentum dependence of the Dyson self energy results in kink type anomalies. In terms of parameter counting, the calculation is *overdetermined*, it can be represented in terms of four parameters which can be fixed from a subset of measurements. With this determination one can then predict many other measurables and testable relations between these- as we show below. We show below that the various predictions are reasonably satisfied in one case (of OPT Bi2212 below), while in other cases, there is insufficient experimental data to test the theories.

The ECFL theory incorporates strong Gutzwiller type correlation effects into the electron dynamics [7]. It produces line shapes that are in close correspondence to experimental results for the high T_c systems [11, 12]. The presence of a low energy kink in the theoretical dispersion was already noted in Ref. (11), the present work substantially elaborates this observation. In order to understand the origin of a low energy scale in the ECFL theory, it is useful to recall the predicted cubic correction to Fermi liquid self energy $\Im m\, \Sigma(\vec{k}_F, \omega) \sim$

$\omega^2(1-\frac{\omega}{\Delta_0})$ from equations (SI-42, 8,9). Here Δ_0 is an emergent low energy scale, it is related to the correlation induced reduction of the quasiparticle weight Z. It reveals itself most clearly in the observed particle hole asymmetry of the spectral functions, and therefore can be estimated independently from spectral *lineshape* analysis. A related and similar low value of the effective Fermi temperature is found in recent studies of the resistivity [10]. Here and in our earlier studies it is coincidentally found that $\Delta_0 \sim 20-50$ meV, i.e. it is also roughly the energy scale of the kinks when the bandwidth is a few eV.

ARPES SPECTRAL DISPERSIONS, KINKS AND A PROTOCOL FOR DATA ANALYSIS

Summary of variables in the theory

A few common features of spectral dispersions found in experiments are summarized in Fig. (1). The schematic figure shows a region of low spectral velocity near the Fermi level followed by a region of steeper velocity, these are separated by a bend in the dispersion-namely the kink. While the kink itself has a somewhat variable shape in different experiments, the "far zone" is much better defined and is usually independent of the temperature, we denote the velocities in the far zones V_L, V_H for the MDC dispersion and the EDC dispersion counterparts by V_L^*, V_H^*. In terms of the normal component of the momentum measured from the Fermi surface

$$\hat{k} = (\vec{k} - \vec{k}_F).\vec{\nabla}\varepsilon_{k_F}/|\vec{\nabla}\varepsilon_{k_F}|, \tag{1}$$

the kink momentum $\hat{k}_{kink}$ is uniquely defined by extrapolating the two asymptotic tangents, and the binding energy at this momentum defines the ideal kink energy E_{kink}^{ideal} (see equation (7)), which serves as a useful reference energy.

Our picture is that all lines of temperature varying MDC dispersion curves in near zone converges into one line in the far zone in Fig. (1). We find that both the low and high velocities are independent of the temperature while depending on the doping levels. Lastly, the new laser ARPES data reveals that we need low temperature dispersion data to determine V_L because temperature effect strongly influences the spectrum near the Fermi level.

We first define the important ratio parameter r $(1 \leq r \leq 2)$ from the MDC dispersion

velocities as

$$r = \frac{2V_H}{V_H + V_L}. \tag{2}$$

The EDC dispersion relation $E^*(\hat{k})$ locates the maximum of the spectral function $A(\vec{k}, \omega)$ in ω at constant $\hat{k}$, while the MDC dispersion and $E(\hat{k})$ locates the maximum $\hat{k}$ at a fixed energy ω. These are found from the ECFL theory (see SI [7] and Ref. (9)) as:

$$E^*(\hat{k}) = \left(r\, V_L \hat{k} + \Delta_0 - \sqrt{\Gamma_0^2 + Q^2} \right), \tag{3}$$

$$E(\hat{k}) = \frac{1}{2-r} \left(V_L \hat{k} + \Delta_0 - \sqrt{r(2-r)\,\Gamma_0^2 + Q^2} \right), \tag{4}$$

where we introduced an energy parameter related to r, V_L and $\hat{k}_{kink}$

$$\Delta_0 = \hat{k}_{kink} V_L (1 - r), \tag{5}$$

and a momentum type variable $Q = (r-1)\, V_L\, (\hat{k} - \hat{k}_{kink})$. The variable Γ_0 is temperature like,

$$\Gamma_0 = \eta + \pi \{\pi k_B T\}^2 / \Omega_\Phi; \tag{6}$$

here η is an elastic scattering parameter dependent upon the incident photon energy, it is very small for laser ARPES experiments and can be neglected to a first approximation. Here Ω_Φ is a self energy decay constant explained further in the SI [7]. The ideal kink energy $V_L \hat{k}_{kink}$ can be expressed in terms of Δ_0 scale as:

$$E_{kink}^{ideal} = -\frac{1}{r-1} \Delta_0. \tag{7}$$

It is important to note that these dispersion relations equations (3,4) are different from the standard dispersion relations $E_{FLT}(\hat{k}) = E^*_{FLT}(\hat{k}) = V_H \hat{k}$, which follow in the simplest Fermi Liquid Theory (FLT) near the Fermi energy $A_{FLT}(\vec{k}, \omega) = \frac{1}{\pi} \frac{\Gamma_0}{(\omega - V_H \hat{k})^2 + \Gamma_0^2}$. The FLT dispersions are identical in EDCs and MDCs, and are independent of the temperature-like variable Γ_0, and do not show kinks. On the other hand equations (3,4) do have kinks- as we show below, and the temperature-like variable Γ_0 plays a significant role in the dispersion. At $\Gamma_0 = 0$ one has an ideal spectrum, where the kinks are sharpest. When $\Gamma_0 \neq 0$, due to either finite temperature or finite damping η, related to the energy of the incoming photon, the kinks are rounded.

A few consequences of equations (3,4) can be noted for the purpose of an experimental determination of the Fermi momentum. The chemical potential is usually fixed by referencing an external metallic contact and is unambiguous. Experimentally the Fermi momentum is usually found from the MDC, as the momentum where the spectral function is maximum with energy fixed at the chemical potential, i.e. $\omega = 0$. This corresponds to the generally wrong expectation, that $E(\hat{k}_{peak}) = 0$ implies $\hat{k}_{peak} = 0$. When $\Gamma_0 \geq 0$, from equation (4) we see that the condition $E(\hat{k}_{peak}) = 0$ gives $\hat{k}_{peak} = \frac{\sqrt{\Delta_0^2 + r^2\,\Gamma_0^2} - \Delta_0}{rV_L}$, a positive number that equals zero only in the ideal case $\Gamma_0 = 0$. Thus there is an apparent enlargement of the Fermi surface due to a finite Γ_0 that needs to be corrected. By the same token, at the true (Luttinger theorem related) Fermi momentum $\hat{k} = 0$, the MDC energy $E(0) = \frac{\Delta_0 - \sqrt{\Delta_0^2 + r(2-r)\Gamma_0^2}}{2-r}$, a negative number when $\Gamma_0 \neq 0$. In recent laser ARPES Bi2201 data Ref. (21) (panel (a) in Fig. (4)), we see that $E(\hat{k}_{peak})$ vanishes at increasing $\hat{k}_{peak}$ as T is raised, as predicted in our calculation. Recent laser ARPES experiment on OPT Bi2212 compounds reports a similar temperature dependence of momentum of MDC dispersion at the Fermi level in Ref. (25), strongly supporting our picture of its origin.

Similarly, the EDC peak at the true Luttinger theorem related Fermi surface $\hat{k} = 0$ is non-zero. We find $E^*(0) = \left(\Delta_0 - \sqrt{\Delta_0^2 + \Gamma_0^2}\right) \leq 0$. Clearly $E^*(0)$ is negative unless $\Gamma_0 = 0$, i.e. it is generically red-shifted. If we are tempted to identify the Fermi momentum from the condition $E^*(\hat{k}^*_{peak}) = 0$, a similar cautionary remark is needed. The condition $E^*(\hat{k}^*_{peak}) = 0$ gives $\hat{k}^*_{peak} = \frac{\sqrt{\Delta_0^2 + (2r-1)\Gamma_0^2} - \Delta_0}{(2r-1)V_L}$, again a positive number as in the MDC case, and thus a slightly different enlargement of the apparent Fermi surface.

The above comments illustrate the difficulty of finding the correct Fermi surface when Γ_0 is non-negligible, as in the case of synchrotron ARPES with substantial values $\Gamma_0 \gtrsim 50$meV. On the other hand the laser ARPES studies have a much smaller $\eta \lesssim 10$ meV, where our analysis can be tested by varying the temperature and the consequent change of the spectrum. In the following, we analyse the data from the Bi2201 system where the laser data is available at various T, and allows us to test the above in detail. Our analysis below of two other synchrotron data, the OPT Bi2212 has $10 \leq \eta \leq 40$ meV, while the low T LSCO data is assumed to be in the limit of $\eta = 0$ because of the lack of high temperature dispersion data.

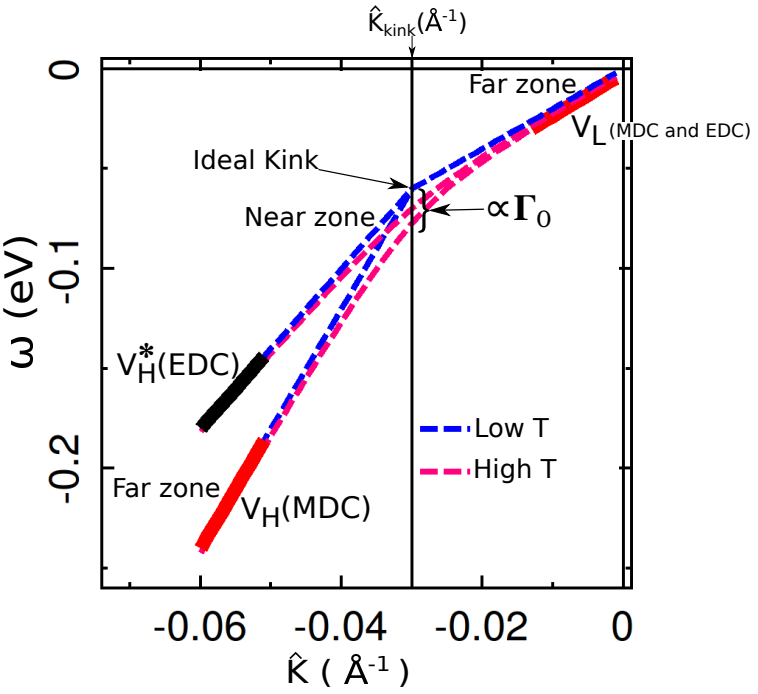

FIG. 1: A schematic MDC and EDC spectrum displaying typical features of experiments discussed below. Here $\hat{k} = (\vec{k} - \vec{k}_F).\vec{\nabla}\varepsilon_{k_F}/|\vec{\nabla}\varepsilon_{k_F}|$, is the momentum component normal to the Fermi surface, and we label EDC variables with a star. (The sketch uses parameters $\mathrm{V_L} = 2\,\mathrm{eV}\,\mathring{A}$, $\mathrm{V_H} = 6\,\mathrm{eV}\,\mathring{A}$, $r = 1.5, \hat{k}_{kink} = -0.03\,\mathring{A}^{-1}$, $\Delta_0 = 0.03\,\mathrm{eV}$, and $\Gamma_0 = 0.01\,\mathrm{eV}$ in equation (3,4)). The tangents in the *far zones* identify the asymptotic velocities $V_L < V_H$ and $V_L^* < V_H^*$ that characterize the MDC and EDC spectra. The intersection of the extrapolated MDC tangents fixes the kink momentum $\hat{k}_{kink}$ and the ideal energy E_{kink}^{ideal}. The dispersion is rounded with raising T, as in the lower (red) curve. We *define* the MDC kink energy E_{kink}^{MDC} as $E(\hat{k}_{kink})$, i.e. the binding energy measured *at* the kink momentum, and similarly the EDC kink energy. In all cases $V_L = V_L^*$. A testable consequence of the ECFL theory is that V_H^* is fixed in terms of the two MDC velocities by a strikingly simple relation: $V_H^* = \frac{3V_H - V_L}{V_H + V_L} \times V_L$. This prediction is tested against experimental data in Fig. (2) where both EDC and MDC data is available. In contrast the electron-Boson theory predicts a jump in the EDC dispersion at the kink energy, followed by $V_H^* = V_H$. Note that the difference between the EDC (MDC) kink energy, $E_{kink}^{EDC} = E_{kink}^{ideal} - \Gamma_0$ and $E_{kink}^{MDC} = E_{kink}^{ideal} - \Gamma_0\sqrt{\frac{r}{2-r}}$, and the ideal kink energy is equal (proportional) to Γ_0

The spectral function at low frequencies close to $\vec{k}_F$ is also obtainable from these parameters, the relevant formula is noted below. In terms of ξ

$$\xi \;=\; \frac{1}{\Delta_0}(\omega - r\, V_L \hat{k}) \tag{8}$$

the spectral function is:

$$A(\vec{k},\omega) = \frac{z_0}{\pi}\frac{\Gamma_0}{(\omega - V_L\hat{k})^2 + \Gamma_0^2} \times \{1 - \frac{\xi}{\sqrt{1 + c_a\xi^2}}\}, \tag{9}$$

Here z_0 is the quasiparticle weight and $c_a \sim 5.4$ (see SI [7]). We should keep in mind that these expressions follow from a low energy expansion, and is limited to small $\hat{k}$ and ω; in practical terms the dimensionless variable $|\xi| \lesssim 4$, so that ω (or $\hat{k}$) is bounded by the kink energy (or momentum), as defined below.

OPT BI2212 ARPES DISPERSION DATA

In the well studied case of optimally doped Bi2212 (BSCCO) superconductors, the kink has been observed in both EDC and MDC. We summarize the ECFL fit parameters in Table (II) obtained from literature [4]. We also display the predicted energy and high velocity of the EDC dispersion. The velocity ratio $V_H/V_H^* \sim 1.3$ in this case, is quite large and measurable. In this case the EDC dispersion has fortunately already been measured, allowing us to test the prediction. From Table (II) we see that the energy of the EDC kink and its velocity are close to the predictions.

MDCs				EDCs			
OPT Bi2212 ARPES data			E_{kink}^{MDC}(meV)	E_{kink}^{EDC}(meV)		V_H^* (eV Å)	
V_L (eV Å)	V_H (eV Å)	$\hat{k}_{kink}$ ($Å^{-1}$)	Calculated	Measured	Calculated	Measured	Predicted	Measured
1.47 ± 0.07	3.3 ± 0.3	-0.037 ± 0.005	67 ± 21	67 ± 8	63 ± 21	65 ± 8	2.60 ± 0.56	2.1 ± 1.1

TABLE II: Parameter table for ARPES kink analysis for OPT Bi2212 [4] in Fig. 2 presents three essential parameters, V_L, V_H, and $\hat{k}_{kink}$. From the high and low temperature MDC dispersions, we measured $\Gamma_0 \lesssim 10$ meV in Panel (b) of Fig. 2. With the measured experimental parameters and determining the velocity ratio r in equation (2), we are able to estimate the finite temperature kink energy for EDC and MDC dispersions by $E_{kink}^{EDC} = E_{kink}^{ideal} - \Gamma_0$ and $E_{kink}^{MDC} = E_{kink}^{ideal} - \Gamma_0\sqrt{\frac{r}{2-r}}$ and predict V_H^* by $V_H^* = \frac{3V_H - V_L}{V_H + V_L} \times V_L$. The uncertainties for calculated variables were determined by error propagation, and the uncertainties for experimental variables were given by the half of the instrumental resolution.

In Panel (a) in Fig. 2, we plot the predicted EDC dispersion using the parameters extracted from the MDC dispersion in Panel (b), and compare with the ARPES data measured[4]. It is interesting that the predicted slope of the EDC dispersion from $V_H^* = \frac{3V_H - V_L}{V_H + V_L} \times V_L$ is close to the measured one. Indeed the measured EDC dispersion is close to that expected from the ECFL theory. To probe further, in Panel (c) in Fig. (2) we compare the theoretical EDC line shape (solid blue line) given by the same parameters through equation (9), with the ARPES line shape measured at high temperature [4]. Panel (d) compares the theoretical MDC curve with the data. The theoretical curves are from the low energy expansion and hence are chopped at the high end, corresponding to roughly $|\xi|_{max} \sim \frac{r\, \mathrm{V_L}\, \hat{k}_{kink}}{\Delta_0}$ for MDC and $|\xi|_{max} \sim \frac{E_{kink}^{ideal}}{\Delta_0}$ for the EDC. With this cutoff, the momentum is less than the kink momentum and the energy is less than the kink energy. We used $\Gamma_0 = 40$ meV since it provides a rough fit for both EDC and MDC spectral functions.

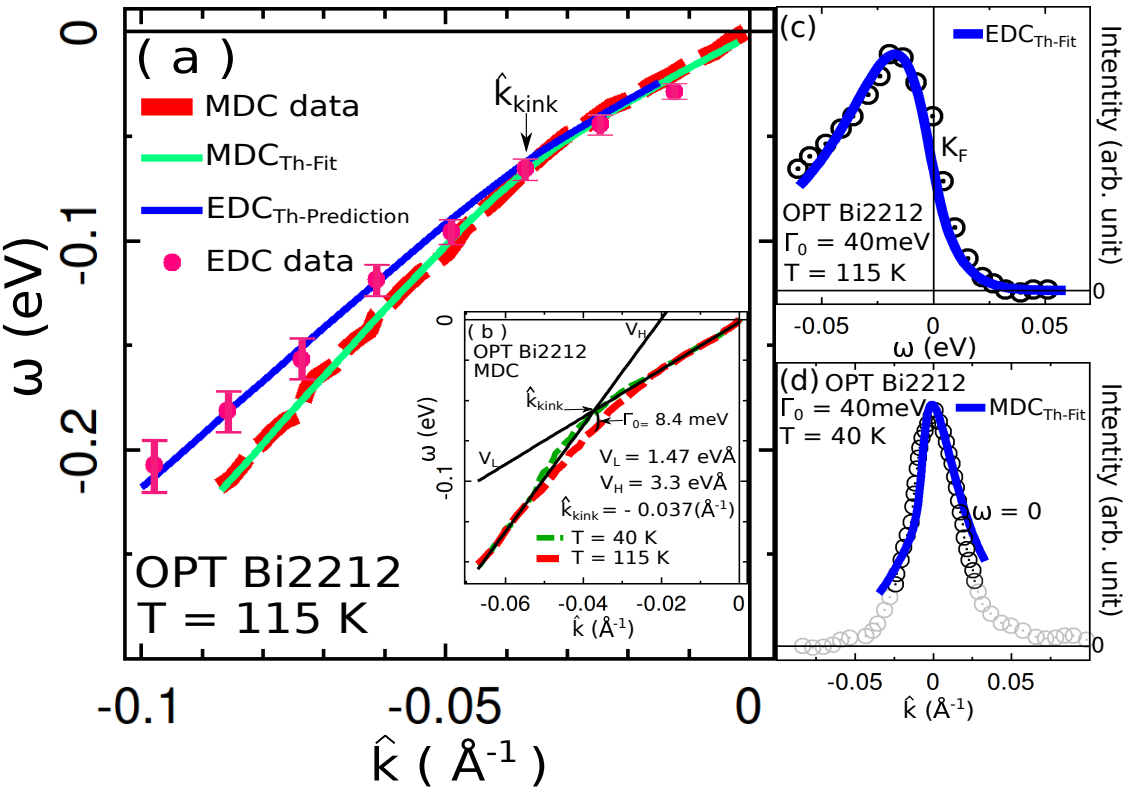

FIG. 2: ARPES kinks data for OPT Bi2212 from Ref. (4) compared to theoretical ECFL curves (solid lines) using parameters listed in Table. II. **Panel:(a)** The predicted EDC spectrum (blue) from equation (3), versus the experimental EDC data (magenta symbols) at T=115K. For reference we also show the MDC data (red dashed curve) and the corresponding ECFL fit (green solid curve). **Panel:(b)** Experimental MDC spectra at 40K (below T_c in green dashed line) and 115K (above T_c in red dashed line) yield common asymptotes shown in black lines from the far zone. These determine the parameters displayed in Table (II). **Panel:(c)** At low energy ± 60 meV, the EDCs spectral function (blue solid line) from equation (9) is contrasted with the corresponding ARPES data from [4]. **Panel:(d)** At $\omega = 0$ we compare the MDCs spectral function (blue solid line) from equation (9) with the corresponding ARPES data from Ref. (4). The range of validity for the theoretical expansion is $\pm\hat{k}_{kink}\,(\,0.037\mathring{A}^{-1}\,)$, the data points in the range are shown in black circle symbols, while the light gray circle symbols are outside this range. The peak position of the theoretical curve has been shifted to left by $0.007\,\mathring{A}^{-1}$, a bit less than the instrumental resolution. A similar shift is made in Panel (l) Fig. 3. For analogous reasons the EDC peak in $A(k,\omega)$ at $\vec{k}_F$ is shifted to the left i.e. $E^*(0) \leq 0$. A small shift to the *right* is made in Panel (k) of Fig. (3), in order to compensate for this effect. These shift effects are within the resolution with present setups, but should be interesting to look for in future generation experiments, since they give useful insights into the energy momentum dependence of the spectral function.

This value is somewhat larger than the bound $\sim$ 10 meV given in Table (II), a smaller value leads to narrower lines but with the same shape. In rigorous terms the same Γ_0 must fit the dispersion and also the spectral functions. Our fit, requiring a different Γ_0, is not ideal in that sense. However the resolution of the available data is somewhat rough, and should improve with the newer experimental setups that have become available. We thus expect that higher resolution data with laser ARPES should provide an interesting challenge to this theory. We also stress that from equation (9), the MDC line shapes look more symmetric than the EDC line shapes at low energies. While many experimental results do show rather symmetric MDCs, there are well known exceptions. For instance MDCs asymmetry has indeed been reported for nearly optimally doped Hg1201 (Tc = 95 K) at binding energy very close to the Fermi level, $\omega \sim$- 5 meV and $\omega \sim$-18 meV in Fig. 5 in Ref. (38). Note that the $\omega = 0$ MDC plot of the spectral function $A(k, \omega)$ from equation (9), locates the peak momentum $\hat{k}_{peak} > 0$, i.e. slightly to the right of the physical Fermi momentum $\vec{k}_F$, and we consider this implies that the *experimental* Fermi momentum determination is subject to such a correction, whenever the spectral function equation (9) has a momentum dependent caparison factor (see caption in Fig. (2)).

LSCO LOW TEMPERATURE DATA

Here we analyze the LSCO data at low temperature (20 K) and at various doping levels raging from the insulator (x = 0.03) to normal metal (x = 0.3) from Ref. (1). The parameters are listed in Table (III), where we observe that the velocity V_L is roughly independent of x, and has a somewhat larger magnitude to that in OPT Bi2212 in Table (II). The kink momentum decreases with decreasing x, roughly as $\hat{k}_{kink} = -(0.37x - 0.77x^2)\mathring{A}^{-1}$, and the kink energies of EDC and MDC dispersions are essentially identical. In the region beyond the kink, the prediction for V_H^* is interesting since it differs measurably from the MDC velocity V_H. We find the ratio $V_H/V_H^* \sim 1.02 - 1.5$ is quite spread out at different doping.

MDCs						EDCs	
LSCO low temperature ARPES data				E_{kink}^{MDC}(meV)		E_{kink}^{EDC}(meV)	V_H^* (eV Å)
x (doping level)	V_L (eV Å)	V_H (eV Å)	$\hat{k}_{kink}$ ($Å^{-1}$)	Calculated	Measured	Calculated Measured	Calculated Measured
0.3	2.4 ± 0.2	3.0 ± 0.3	-0.047 ± 0.005	113 ± 29	110 ± 10	113 ± 29	2.93 ± 0.45
0.22	2.0 ± 0.1	3.6 ± 0.2	-0.042 ± 0.005	84 ± 18	85 ± 10	84 ± 18	3.14 ± 0.35
0.18	1.7 ± 0.3	4.5 ± 0.6	-0.040 ± 0.005	68 ± 43	72 ± 10	68 ± 43	3.2 ± 1.2
0.15	1.75 ± 0.07	4.3 ± 0.1	-0.037 ± 0.005	65 ± 11	64 ± 10	65 ± 11	3.23 ± 0.20
0.12	2.0 ± 0.3	3.7 ± 0.5	-0.029 ± 0.005	58 ± 28	55 ± 10	58 ± 28	3.19 ± 0.89
0.1	1.8 ± 0.2	5.0 ± 0.7	-0.035 ± 0.005	63 ± 44	64 ± 10	63 ± 44	3.5 ± 1.4
0.075	1.9 ± 0.2	5.6 ± 0.8	-0.026 ± 0.005	49 ± 37	51 ± 10	49 ± 37	3.8 ± 1.7
0.063	1.8 ± 0.3	6.0 ± 0.5	-0.022 ± 0.005	40 ± 21	43 ± 10	40 ± 21	3.7 ± 1.1
0.05	1.7 ± 0.2	5.7 ± 0.6	-0.023 ± 0.005	39 ± 25	41 ± 10	39 ± 25	3.5 ± 1.3
0.03	2.0 ± 0.3	6.1 ± 0.4	-0.016 ± 0.005	32 ± 15	32 ± 10	32 ± 15	4.02 ± 0.85

TABLE III: Data table for ARPES kink analysis for OPT LSCO (T = 20 K) [1] in Fig. 3. We were unable to reliably estimate Γ_0 here due to the lack of data at high temperature, and hence set it at zero. The uncertainties for measured values were given by half of the instrumental resolution (10 meV, $\sim 0.005\, Å^{-1}$). The uncertainties for the calculated values were determined by error propagation.

Our analysis becomes unreliable as lower doping level x $<$ 0.075 in Panels (h) to (j) in Fig. 3, where the dispersion kink is no longer a simple bending kink, an extra curving tendency begins to appear. To put this in context, recall that the line shape of LSCO becomes extremely broad at small x [14], and so the peak position of the spectral function becomes more uncertain than at higher energy. We should point out that in Fig. (3) Panel

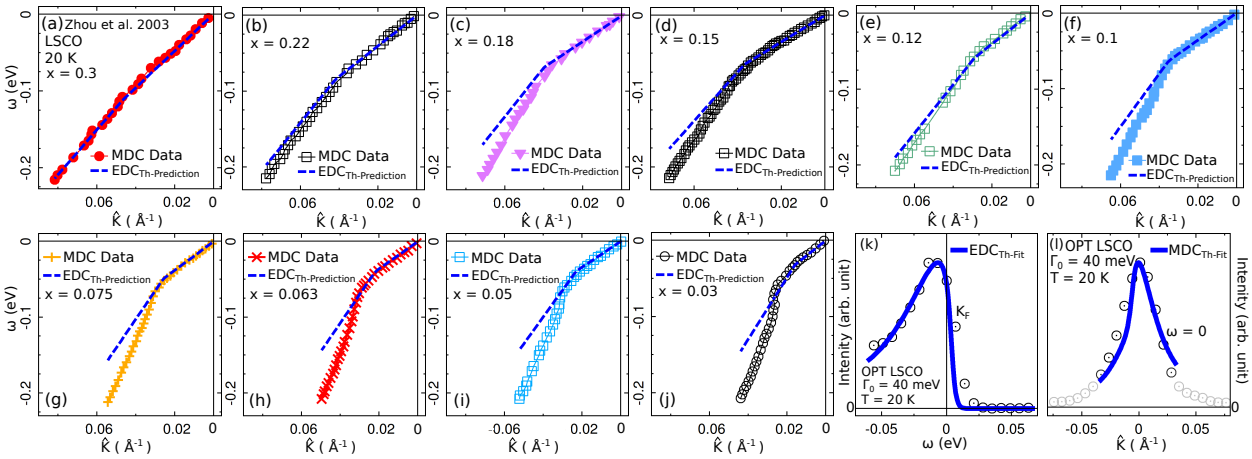

FIG. 3: ARPES kinks data for LSCO data [1] compared to theoretical ECFL curves (solid lines) using parameters listed in Table. III. The doping level x varies between (normal metal) 0.3 $\leq$ x $\leq$ 0.03 (insulator) in Panels (a) to (j). Each panel shows MDC nodal dispersion data (symbols), whose uncertainties are $\pm$ 10 meV. The blue dashed line is the theoretical prediction for EDC dispersion by equation (3). **Panel:(k)** We compare the spectral line shape for EDCs at k_F from equation (9) (blue solid line) in the range $\pm\, E^{ideal}_{kink} \sim$ 65 meV with the corresponding ARPES data (black circles) [12]. **Panel:(l)** At $\omega = 0$ we compare the MDCs spectral function (blue solid line) from equation (9) with the corresponding ARPES data from Ref. (12). The range of validity for the theoretical expansion is $\pm\, \hat{k}_{kink}\, (0.037 \mathring{A}^{-1})$, the data points in the range are shown in black circle symbols, while the light gray circle symbols are outside this range. The peak position of the theoretical curve MDC has been shifted to left by 0.006 $\mathring{A}^{-1}$.

(k) the spectral function has been shifted to right by 4 meV for a better fit. This shifting is consistent with our argument that the Fermi momentum determination has a possible small error of in order 0.006 $\mathring{A}^{-1}$, arising from the $\hat{k}$ dependent caparison factor, and hence the peak position has an uncertainty $V_L \times .006 \sim 10$ meV.

BI2201 LASER ARPES DATA

In this section, we present our analysis of the high resolution laser ARPES data of the single layered compounds Bi2201, at various different doping levels taken from a recent study in Ref. (21). In earlier studies of this compound using synchrotron emitted high energy photons, as also LSCO [3], the ARPES kinks were observed to have only a weak temperature dependence [5]. However, the new high resolution laser ARPES data enables us to observe clear and significant temperature dependence of the ARPES kinks; it is comparable to that of the double layered Bi2212 compounds. In fact we find that the new data of Bi2201 compounds in Ref. (21) seems to provide a textbook example of our ECFL kink analysis.

In Table(IV) we list the kink parameters corresponding to different doping levels of Bi2201 and tabulate the kink parameters. The entries are in correspondence to the panels in Fig. (4). In Fig. (4) panels (a) to (f), we depict the measured MDC dispersion and the predicted EDC dispersions at different doping levels. The latter are found from equation (3) using the variables in Table (IV). Panels (g) and (h) of OPT Bi2201 are especially interesting. Combining the low $T = 15$K dispersion data and the finite T value of Γ_0, found from the depression of the kink energy $E_{kink}^{MDC} = E_{kink}^{ideal} - \Gamma_0\sqrt{\frac{r}{2-r}}$, we can reconstruct the entire MDC dispersion at a finite T. This may be compared with the measured finite T MDC data, thus checking the validity of the formalism. This exercise is carried out at T=200K in Panel (g) and T=100 K in panel (h), where we find a remarkably good fit in all details. In panels (g,h) we show the actual momentum (rather than $\hat{k}$) to facilitate a comparison with data. Panel (g) especially clearly shows that $E(\hat{k})$ vanishes at a $\hat{k}$ that is different from 0. The shift corresponds to $\sim 0.01\mathring{A}^{-1}$. We have commented above that this apparent expansion of the Fermi surface with T is due to the non trivial physics underlying equation (4) lying beyond the simple minded FLT.

Panel (i) in Fig. (4) plots the temperature dependence of Γ_0 in panel (a) in Fig.(4) in Ref. (21). The measured Γ_0 curve is fitted with equation (6), and we estimate $\eta = 5.3 \pm 2$ meV and $\Omega_\Phi = 410 \pm 100$ meV.

MDCs						EDCs	
Bi2201 laser ARPES data				E_{kink}^{MDC}(meV)		E_{kink}^{EDC}(meV)	V_H^* (eV Å)
x (doping level)	V_L (eV Å)	V_H (eV Å)	k_{kink} ($Å^{-1}$)	Calculated	Measured	Calculated Measured	Calculated Measured
0.1	1.47 ± 0.12	4.7 ± 0.3	-0.022 ± 0.002	32 ± 3	37 ± 0.5	32 ± 6	3.0 ± 0.3
0.11	1.34 ± 0.06	2.78 ± 0.06	-0.021 ± 0.002	28 ± 1	28 ± 0.5	28 ± 4	2.28 ± 0.12
0.13	1.37 ± 0.07	2.71 ± 0.18	-0.025 ± 0.002	38 ± 3	39 ± 0.5	37 ± 5	2.27 ± 0.17
0.16	1.5 ± 0.1	3.5 ± 0.2	-0.026 ± 0.002	39 ± 3	43 ± 0.5	39 ± 6	2.7 ± 0.2
0.23	2.1 ± 0.11	5.4 ± 0.3	-0.036 ± 0.002	98 ± 6	97 ± 0.5	89 ± 10	3.9 ± 0.3
0.26	2.17 ± 0.16	4.8 ± 0.4	-0.045 ± 0.002	123 ± 11	122 ± 0.5	114 ± 18	3.8 ± 0.4
0.16 (200 K)	1.61 ± 0.18	3.5 ± 0.3	0.364 ± 0.002	87 ± 11	89 ± 0.5	75 ± 11	2.8 ± 0.4
0.16 (100 K)	1.61 ± 0.18	3.5 ± 0.3	0.364 ± 0.002	69 ± 11	70 ± 0.5	62 ± 11	2.8 ± 0.4

TABLE IV: Parameter table for ARPES kink analysis for laser ARPES data of Bi2201 at various different doping levels [21] in Fig.4. From $0.1 < x < 0.16$, we measured $\Gamma_0 \sim 0$. For $x = 0.23$ and 0.26, we measured $\Gamma_0 \lesssim 17$ meV. For $x = 0.16$ data, we report variables for high temperature kinks data 200 K (g) and 100 K (h) in Fig. (4), and Γ_0 values for 200 K and 100 K data are in corresponding panels (g) and (h) in Fig. (4). The uncertainties for the calculated parameters were determined by error propagation, and the uncertainties for the experimental parameters were given by half of the instrumental resolution.

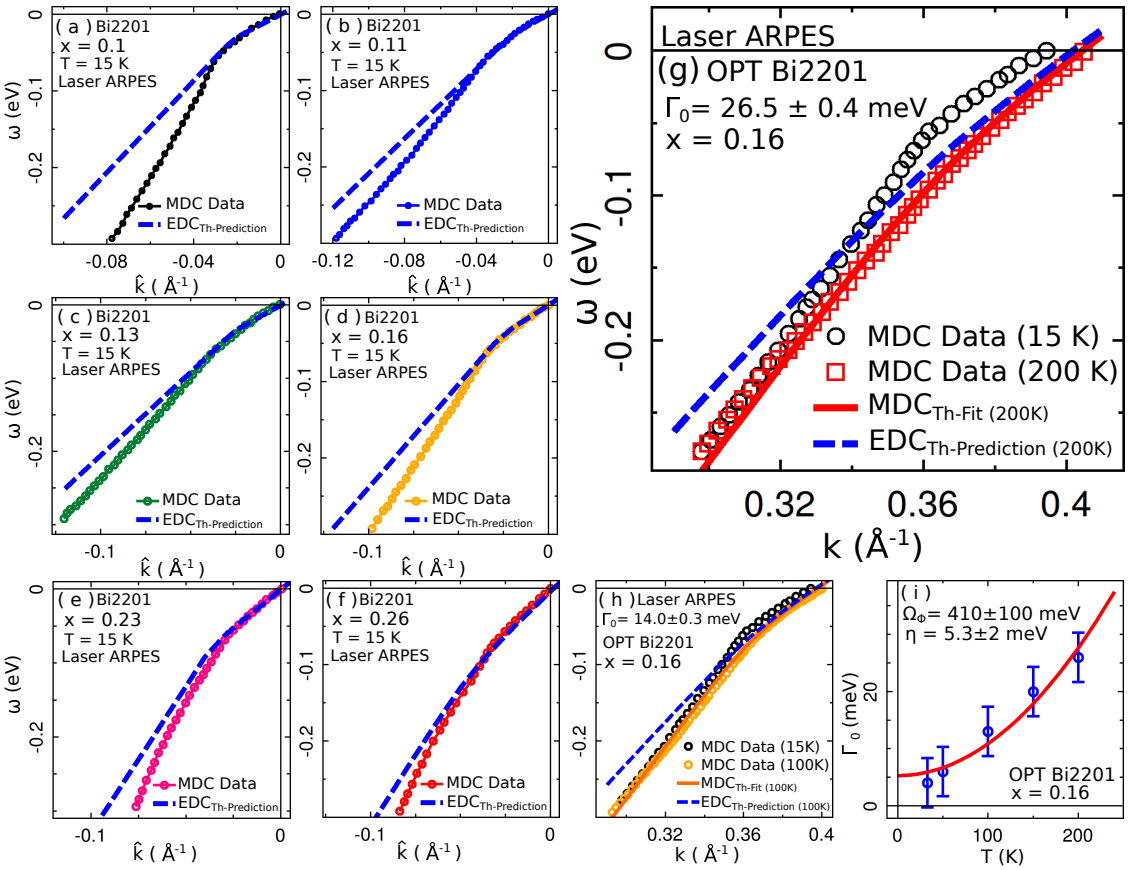

FIG. 4: ARPES kink analysis for laser ARPES data of Bi2201 at various different doping levels in Ref. (21). **Panels:(a) to (f)** we predict EDC dispersions (blue dashed lines) using equation (3) for various different doping levels of Bi2201 laser ARPES data. **Panel:(g) and (h)** we predict high temperature EDC (blue dashed lines) dispersions (g) 200K and (h) 100K for laser ARPES data of OPT Bi2201 (panel (a) in Fig.4 in Ref. (21)), and show the MDC dispersion fits for two temperature also. We estimate Γ_0 from measuring the difference between the ideal kink energy and the MDC kink energy. In order to compare with experiments, the x-axis representation in (g) and (h) are given by the physical k (rather than the momentum difference $\hat{k}$). In panel (g), the MDC dispersion fit of 200 K vanishes at $k = 0.404 \pm 0.002\,\mathring{A}^{-1}$, very close to the measured $k = 0.405 \pm 0.002\,\mathring{A}^{-1}$ of the MDC dispersion data at 200 K. Similarly in panel (h) the MDC dispersion fit at 100 K vanishes at $k = 0.398 \pm 0.002\,\mathring{A}^{-1}$, close to the measured $k = 0.4 \pm 0.002\mathring{A}^{-1}$ of the MDC dispersion data at 100 K. Note that the true fermi momentum as estimated from the low T (15 K) data is $k = 0.394 \pm 0.002\,\mathring{A}^{-1}$, so that the deviations are bigger than the momentum resolution $\Delta k \sim 0.004\,\mathring{A}^{-1}$. **Panel:(i)** we plot the temperature dependence of Γ_0 in panel (a) in Fig.4 in Ref. (21). Here, the temperature dependence data of Γ_0 is fitted with equation (6), and η is determined 5.3 ± 2 meV and $\Omega_\Phi = 410 \pm 100$ meV.

CONCLUSION

The main goal of this work is to understand the physical origin of kinks in the dispersion seen in ARPES studies of a wide class of systems. For this purpose we have listed fifteen systems of topical interest where ARPES kink data is available. Our focus is on the nodal direction data, since the largest volume is available here. We have devised a useful protocol to extract kink parameters from data, where the asymptotic tangents of the kink are used. Using this protocol we have analyzed in detail three families of systems, two synchrotron and one laser ARPES data of cuprate superconductors. The main parameters of the kinks are the energy, momentum and the dispersion velocities in EDC and MDC scans, these provide a quantitative data set for testing various theoretical proposals for explaining kinks.

We have outlined two competing theories for the origin of kinks, and highlighted their distinctive predictions. One is the electron-Boson model, where an Einstein mode of either spin or charge origin couples to the electrons, resulting in a momentum independent self energy. This theory gives rise to kinks in the electron dispersion. The other theory is the strong or extreme correlation theory, where the interactions lead to a momentum dependent self energy in two dimensions. This theory also gives rise to kinks in the electron dispersion.

The predictions of the two theories differ significantly and in experimentally testable ways. The Boson-mode theory gives rise to kinks located *at* the energy of the localized mode. For the kinks, the Boson-mode theory predicts [7]: (1) a momentum independent peak in the spectral function at the kink energy when $\hat{k} < \hat{k}_{kink}$, (2) a jump in the EDC dispersion at the kink energy but not the MDC dispersion and (3) the EDC and MDC velocities are identical both before and after the kink is crossed.

The extremely strong correlation theory also gives rise to kinks in dispersion, these originate from the momentum dependence of the self energy [7]. A simple low energy and momentum expansion of the ECFL theory gives inter-relations between observed features of the kinks. It predicts (1) a kink at an emergent low energy scale originating from Gutzwiller correlations (2) no jump in the EDC dispersion and (3) the EDC velocity is determined by the MDC velocities through $V_H^* = \frac{3V_H - V_L}{V_H + V_L} \times V_L$. It is remarkable that a knowledge of the MDC dispersion suffices to predict the EDC dispersion, and the parameters obtained from the MDC dispersion enable us to reconstruct the spectral function at low momentum and energy, in both MDC and EDC scans.

It is thus clear that EDC dispersions hold the key to distinguishing between the two competing theories. EDC dispersion data is sparse but exists, the work on OPT Bi2212 from Ref. (4) shown in Fig. (2), presents both EDC and MDC dispersions at 115 K. Its resolution is presumably not optimal, since it was an early experiment. Nevertheless we can use it to make a first pass at comparing the two theories. This data set plotted in Fig. (2) shows that the EDC dispersion is continuous, i.e. has no jump. Further the EDC higher velocity V_H^* is close to that predicted by the ECFL analysis. The measured spectral function in EDC, overlooking the noise, seem not to have any immovable feature at E_{kink}. Thus all three characteristics noted above appear to be consistent with the ECFL predictions rather than the Bosonic mode theory predictions. It is roughly fit by the low energy parameterized curves as well, where the MDC is seen to be more symmetric than the EDC cuts.

As noted in Table (I) the above case OPT Bi2212 is particularly interesting. Low energy Bosonic modes have been observed in neutron scattering [27, 28], and in momentum resolved electron energy loss experiments [26]. In Ref. (26) an MDC dispersion is presented using parameters taken from the Bosonic data. This leads to a rather detailed model, and is shown to provide a reasonable fit to the MDC dispersion and the observed kink, but the important EDC dispersion is not displayed.

While we focussed attention on dispersion kinks in the nodal direction in the present work, the ECFL theory is also valid for other directions, it has a momentum dependence in the self energy both normal to the Fermi surface and also along the tangent. The ECFL theory applied to the d-wave superconducting state in the t-J model is expected to lead to further interesting results in the future. For now we note that the observed nodal direction spectra are essentially unchanged at T_c, which makes the nodal direction particularly interesting.

In conclusion, we have presented a current summary of the physics of the kinks in dispersion of cuprate high Tc superconductors. We believe that there is urgent need for further high resolution EDC data, and also T dependent scans to explore the rounding of kinks. Using such data one should be able to check the predictions of the theory more thoroughly, and thereby obtain definitive understanding of the origin of low energy ARPES kinks of strongly correlated matter.

ACKNOWLEDGEMENTS

We thank Antoine Georges and Jason Hancock for stimulating discussions. The work at UCSC was supported by the U.S. Department of Energy (DOE), Office of Science, Basic Energy Sciences (BES) under Award # DE-FG02-06ER46319.

[1] Zhou, X-J., *et al.* High-temperature superconductors: universal nodal Fermi velocity. *Nature* **423**.6938 (2003): 398-398.

[2] Johnson, P. D., *et al.* Doping and temperature dependence of the mass enhancement observed in the cuprate Bi2 Sr2 CaCu2 $O_{8+\delta}$. *Physical Review Letters* **87**.17 (2001): 177007.

[3] Lanzara, A., *et al.* Evidence for ubiquitous strong electronphonon coupling in high-temperature superconductors. *Nature* **412**.6846 (2001): 510-514.

[4] Kaminski, A., *et al.* Renormalization of spectral line shape and dispersion below Tc in Bi2 Sr2 CaCu2 $O_{8+\delta}$. *Physical Review Letters* **86**.6 (2001): 1070.

[5] Sato, T., *et al.* Observation of band renormalization effects in hole-doped high-T c superconductors. *Physical Review Letters* **91**.15 (2003): 157003.

[6] He, J. *et. al.*, Coexistence of Two Sharp-Mode Couplings and their Unusual Momentum Dependence in the Superconducting State of Bi2 Sr2 CaCu2 $O_{8+\delta}$ Revealed by Laser-Based Angle-Resolved Photoemission, *Physical Review Letters* **111**.10 (2013): 107005.

[7] Supplementary Information

[8] Shastry, B. Sriram. Extremely correlated Fermi liquids. *Physical Review Letters* **107**.5 (2011): 056403.

[9] Shastry, B. Sriram. Theory of extreme correlations using canonical Fermions and path integrals. *Annals of Physics* **343** (2014): 164-199.DOI:http://dx.doi.org/10.1016/j.aop.2014.02.005. (Erratum) *Ann. Phys.* **373**, 717-718 (2016). DOI:http://dx.doi.org/10.1016/j.aop.2016.08.015.

[10] Shastry, B. Sriram, and Edward Perepelitsky. Low-energy physics of the t-J model in $d = \infty$ using extremely correlated Fermi liquid theory: Cutoff second-order equations. *Physical Review B* **94**.4 (2016): 045138.

[11] Gweon, G-H., B. S. Shastry, and G. D. Gu. Extremely Correlated Fermi-Liquid Description of Normal-State ARPES in Cuprates. *Physical Review Letters* **107**.5 (2011): 056404.

[12] Matsuyama, K, and Gweon, G-H. Phenomenological Model for the Normal-State Angle-Resolved Photoemission Spectroscopy Line Shapes of High-Temperature Superconductors. *Physical Review letters* **111**.24 (2013): 246401.

[13] Garcia, D. R., and A. Lanzara. Through a Lattice Darkly: Shedding Light on Electron-Phonon Coupling in the High Tc Cuprates. *Advances in Condensed Matter Physics* 2010 (2010).

[14] Yoshida, T., *et al.* Low-energy electronic structure of the high-Tc cuprates $La_{2-x}Sr_xCuO4$

studied by angle-resolved photoemission spectroscopy. *Journal of Physics: Condensed Matter* **19**.12 (2007): 125209.

[15] Mishchenko, A. S., *et al.* Polaronic metal in lightly doped high-Tc cuprates. *EPL (Europhysics Letters)* **95**.5 (2011): 57007.

[16] McQueeney, R. J., *et al.* Anomalous dispersion of LO phonons in La1.85 Sr0.15 CuO4 at low temperatures. *Physical Review Letters* **82**.3 (1999): 628.

[17] Pintschovius, L., and M. Braden. Anomalous dispersion of LO phonons in La1.85 Sr0.15 CuO4. *Physical Review B* **60**.22 (1999): R15039.

[18] Fukuda, T., *et al.*Doping dependence of softening in the bond-stretching phonon mode of La_{2-x} Srx CuO4 ($0 \leq x \leq 0.29$).*Physical Review B* **71**.6 (2005): 060501.

[19] Vignolle, B., *et al.* Two energy scales in the spin excitations of the high-temperature superconductor $La_{2?x}$SrxCuO4. *Nature Physics* **3**.3 (2007): 163-167.

[20] Yang, K., *et al.* Normal-state electronic structure in the heavily overdoped regime of Bi1.74 Pb0.38 Sr1.88 Cu $O_{6+\delta}$ single-layer cuprate superconductors: An angle-resolved photoemission study. *Physical Review B* **73**.14 (2006): 144507.

[21] Ying-Ying, Peng, et al. Doping Evolution of Nodal Band Renormalization in Bi2Sr2Cu$O_{6+\delta}$ Superconductor Revealed by Laser-Based Angle-Resolved Photoemission Spectroscopy. *Chinese Physics Letters* **30**.6 (2013): 067402.

[22] Meevasana, W., *et al.* Hierarchy of multiple many-body interaction scales in high-temperature superconductors. *Physical Review B* **75**.17 (2007): 174506.

[23] Graf, Jeff, *et al.* Bond stretching phonon softening and kinks in the angle-resolved photoemission spectra of optimally doped Bi2 Sr1.6 La0.4 Cu2 $O_{6+\delta}$ superconductors. *Physical Review Letters* **100**.22 (2008): 227002.

[24] Bogdanov, P. V., *et al.* Evidence for an energy scale for quasiparticle dispersion in Bi2 Sr2 CaCu2 O8. *Physical Review Letters* **85**.12 (2000): 2581.

[25] Zhang, Wentao, et al. Identification of a new form of electron coupling in the Bi2Sr2CaCu2O8 superconductor by laser-based angle-resolved photoemission spectroscopy. *Physical Review Letters* **100**.10 (2008): 107002.

[26] Vig, Sean, *et al.* Low-energy bosonic modes in a high-temperature superconductor with incipient charge order. arXiv preprint arXiv:1509.04230 (2015).

[27] Fong, H. F., *et al.* Neutron scattering from magnetic excitations in Bi2Sr2CaCu2$O_{8+\delta}$. *Nature*

398.6728 (1999): 588-591.

[28] He, H., *et al.* Resonant spin excitation in an overdoped high temperature superconductor. *Physical Review Letters* **86**.8 (2001): 1610.

[29] Ideta, S., *et al.* Anisotropy of gap and kink energies in the trilayer high-Tc cuprate superconductor Bi2Sr2Ca2Cu3O$_{10+\delta}$. *Journal of Physics: Conference Series* **108**.1 (2008).

[30] Ideta, S., *et al.* Effect of electron-phonon coupling in the ARPES spectra of the tri-layer cuprate Bi2Sr2Ca2Cu3O$_{10+\delta}$. *Journal of Physics: Conference Series* **428**.1 (2013).

[31] Borisenko, S. V., *et al.* Kinks, nodal bilayer splitting, and interband scattering in YBa2 Cu3 O$_{6+x}$. *Physical Review Letters* **96**.11 (2006): 117004.

[32] Reichardt, W., *et al.* Phonons in YBa2Cu3O$_{7-\delta}$. *Physica C: Superconductivity* **162** (1989): 464-465.

[33] Pintschovius, L., *et al.* Oxygen phonon branches in YBa2 Cu3 O7. *Physical Review B* **69**.21 (2004): 214506.

[34] Rossat-Mignod, J., *et al.* Neutron scattering study of the YBa2 Cu3 O$_{6+x}$ system. *Physica C: Superconductivity* **185** (1991): 86-92.

[35] Mook, H. A., *et al.* Polarized neutron determination of the magnetic excitations in YBa2 Cu3 O$_7$. *Physical Review Letters* **70**.22 (1993): 3490.

[36] Dai, P., *et al.* Magnetic Dynamics in Underdoped YBa2 Cu3 O$_{7-x}$: Direct Observation of a Superconducting Gap. *Physical Review Letters* **77**.27 (1996): 5425.

[37] Dai, Pengcheng, *et al.* Evolution of the resonance and incommensurate spin fluctuations in superconducting YBa2 Cu3 O$_{6+x}$. *Physical Review B* **63**.5 (2001): 054525.

[38] Vishik, I. M., *et al.* Angle-resolved photoemission spectroscopy study of Hg Ba2 CuO$_{4+\delta}$. *Physical Review B* **89**.19 (2014): 195141.

[39] dAstuto, Matteo, *et al.* Phonon dispersion in the one-layer cuprate HgBa2CuO$_{4+\delta}$. *Journal of Physics: Condensed Matter* **15**.50 (2003): 8827.

[40] Li, Yuan, *et al.* Hidden magnetic excitation in the pseudogap phase of a high-Tc superconductor. *Nature* **468**.7321 (2010): 283-285.

[41] Li, Yuan, *et al.* Two Ising-like magnetic excitations in a single-layer cuprate superconductor. *Nature Physics* **8**.5 (2012): 404-410.

[42] Chan, M. K., *et al.* Commensurate antiferromagnetic excitations as a signature of the pseudogap in the tetragonal high-Tc cuprate HgBa2CuO$_{4+\delta}$. *Nature Communications* **7** (2016).

[43] Chen, Yulin, *et al.* Unusual layer-dependent charge distribution, collective mode coupling, and superconductivity in multilayer cuprate Ba2 Ca3 Cu4 O8 F2. *Physical Review Letters* **103**.3 (2009): 036403.

[44] Ronning, F., *et al.* Evolution of a metal to insulator transition in $Ca_{2-x}Na_x$ Cu O2 Cl2 as seen by angle-resolved photoemission. *Physical Review B* **67**.16 (2003): 165101.

[45] Mannella, Norman, *et al.* Nodal quasiparticle in pseudogapped colossal magnetoresistive manganites.*Nature* **438**.7067 (2005): 474-478.

[46] Valla, T., *et al.* Charge-density-wave-induced modifications to the quasiparticle self-energy in 2H-TaSe 2. *Physical Review Letters* **85**.22 (2000): 4759.

[47] Brusdeylins, G., *et al.* He-atom scattering study of the temperature-dependent charge-density-wave surface structure and lattice dynamics of 2H-TaSe2 (001). *Physical Review B* **41**.9 (1990): 5707.

[48] Schafer, J., *et al.* Electronic quasiparticle renormalization on the spin wave energy scale. *Physical Review Letters* **92**.9 (2004): 097205.

[49] Brouet, V., *et al.* Measuring Fermi velocities with ARPES in narrow band systems: The case of layered cobaltates. *Journal of Electron Spectroscopy and Related Phenomena* **185**.5 (2012): 146-151.

arXiv:1610.08079v2 [cond-mat.str-el] 15 Dec 2016

Supplementary Information: Origin of Kinks in Energy Dispersion of Strongly Correlated Matter

Kazue Matsuyama,[1] Edward Perepelitsky,[2,3] and B Sriram Shastry[1]

[1]*Physics Department, University of California, Santa Cruz, CA 95064*

[2]*Centre de Physique Théorique, École Polytechnique, CNRS, Université Paris-Saclay, 91128 Palaiseau, France*

[3]*Collège de France, 11 place Marcelin Berthelot, 75005 Paris, France*

(Dated: December 19, 2016)

In this supplemental note we provide (I) some details of the doping dependence of the fit parameters (II) detailed predictions of the electron-Boson coupling model for kinks and (III) detailed predictions of the extremely strong correlation theory for kinks. In the main paper, we have discussed alternate mechanisms for generating the low-energy kink observed in ARPES. Although both mechanisms are capable of generating similar MDC dispersions, they produce EDCs and EDC dispersions which are distinct from one another in several clearly identifiable ways. These differences, detailed below, can be used to distinguish between the two mechanisms using ARPES, especially as higher resolution data becomes available in the future.

Fixing the parameters

The independent parameters in the ECFL expressions for the kink can be taken as $V_H, V_L, \hat{k}_{kink}$ and Γ_0. These can be fixed with four measurements as we indicate below. While the first three can be measured with precision, the variable Γ_0 depends on the temperature and is also quite sensitive to the various experimental conditions including the incident photon energy, thus making it less precisely known than the others; we will perforce be content with rough estimates of this variable. The remaining parameters can be calculated using equation (MS-2) and equation (MS-5) etc. As mentioned above, the theory is overdetermined, in terms of these four parameters, the theory predicts a number of other quantities: a) the dispersion curves for both EDCs and MDCs, b) the location of both EDC and MDC kinks at finite temperature, and c) the spectral functions near the Fermi level (up to roughly the kink energy). Below we present an analysis of the ARPES data of Bi2212, LSCO and Bi2201 taken from literature, where we give the details of the fits and the predicted EDC velocities for future experiments.

The asymptotic velocities V_H, V_L determine the ratio r from equation (MS-2). The energy Δ_0 and the ideal kink energy are determined from equations (MS-5, SI-28). As discussed in Fig. 1 E_{kink}^{MDC} is found by measuring the dispersion at the kink wave vector $E(\hat{k}_{kink})$, and similarly the EDC kink energy E_{kink}^{EDC} is found from $E^*(\hat{k}_{kink})$. For understanding the finite temperature data, the theory provides temperature dependent correction terms for the two

spectra, determined by the parameter Γ_0,

$$E_{kink}^{EDC} = E_{kink}^{ideal} - \Gamma_0, \tag{SI-1}$$

$$E_{kink}^{MDC} = E_{kink}^{ideal} - \Gamma_0 \sqrt{\frac{r}{2-r}}. \tag{SI-2}$$

Since Γ_0 determines the non-zero T (or η) correction, we estimate from the difference between low and high temperature MDC dispersion curves

$$\Gamma_0 = \Delta E_{kink} = \sqrt{\frac{2-r}{r}} \left(E_{kink}^{ideal} - E_{kink}^{MDC} \right). \tag{SI-3}$$

Clearly uncertainties in Γ_0 are governed by those in the MDC dispersion at the kink momentum.

As noted in Fig. 1, the ECFL theory predicts a kink, rather than a jump in the EDC spectrum, quite analogous to that in the MDC dispersion, but with a different velocity on the steeper side, i.e. $V_H^* \neq V_H$. In fact the theory provides an experimentally testable expression relating the two, V_H^* is expressed quite simply in terms of measurable experimental variables,

$$V_H^* = \frac{3V_H - V_L}{V_H + V_L} \times V_L. \tag{SI-4}$$

As mentioned in the introduction the Boson-mode coupled theories predict a jump in the EDC spectrum at the kink energy. The velocity beyond the jump is the same in EDC and MDC, i.e. $V_H^* = V_H$, in contrast to Eq. (SI-4). This velocity is reported in only a few cases, and provides a ready test of the ECFL theory.

The theory also predicts $V_L = V_L^*$, which is satisfied by inspection in all reported cases and is common to the Boson-mode theory. We use this protocol to analyze the experiments on three well studied families of high T_c materials next.

Fit parameters

(I) Δ_0 for LSCO data in the main text For the LSCO data discussed in the main text, we quoted the ECFL theory parameters, velocity ratio r, the ideal kink energy E_{kink}^{ideal} and the small energy parameter Δ_0, in Eqs (1,6,4) (see also Eq. (SI-28)). In Fig. 1, we display the doping dependence of these parameter $x = 1 - n$. The size of the data point represent the uncertainty for each data points. While r and Δ_0 stay almost constant, the ideal kink energy decreases linearly with increasing x.

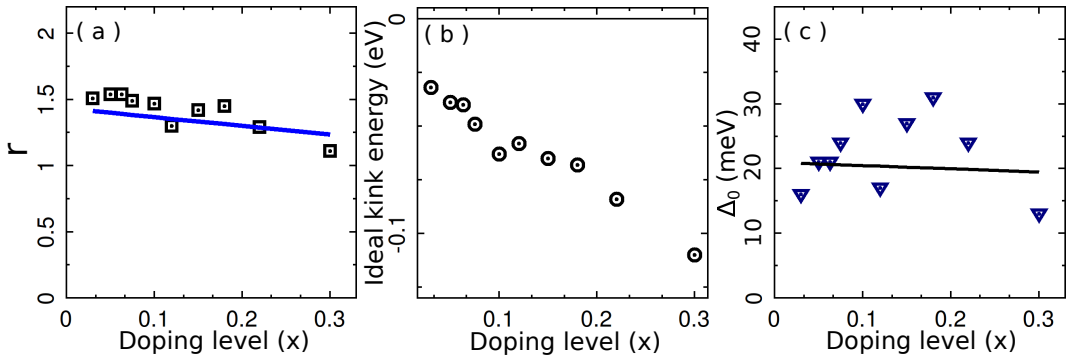

FIG. 1: (a) The ratio of low and high velocities, r, as a function of doping levels, and (b) ideal kink energy, (c) ECFL energy parameter Δ_0 as a function of doping levels for LSCO data in the main text.

(II) ELECTRON-BOSON COUPLING THEORY OF KINKS

The electron Boson mechanism suggested in Ref. (2) and others [3, 4], is the coupling of the electrons to Bosonic modes (such as phonons), located at the kink energy. To illustrate the basic idea, we first consider free electrons coupled to an Einstein phonon mode of energy $\omega_0 = .08$ eV [3, 4], with coupling constant g. In this case, the spectral function is expressed in terms of a momentum independent self-energy $\Sigma(\omega)$, as

$$A(\vec{k},\omega) = -\frac{1}{\pi}\frac{\Im m\Sigma(\omega)}{(\omega - \xi_k - \Re e\Sigma(\omega))^2 + (\Im m\Sigma(\omega))^2}, \tag{SI-5}$$

where $\xi_k \equiv \varepsilon_k - \mu$, ε_k is the bare dispersion, and μ is the chemical potential. The real and imaginary parts of the self-energy due to the electron-phonon interactions are given by the well known formulas: [5, 6]

$$\begin{aligned} \Im m\Sigma(\omega) &= -\pi g^2 \sum_{\pm} N(\omega + \mu \pm \omega_0) \times \\ &\quad \left[f^{\mp}(\omega \pm \omega_0) + n(\omega_0)\right], \\ \Re e\Sigma(\omega) &= -\frac{1}{\pi}\int d\nu \frac{\Im m\Sigma(\nu)}{\omega - \nu}, \end{aligned} \tag{SI-6}$$

where $f^-(\nu) \equiv f(\nu)$, $f^+(\nu) \equiv \bar{f}(\nu) \equiv 1 - f(\nu)$, $f(\nu)$ and $n(\nu)$ are the Fermi and Bose distribution functions respectively, and $N(E) \equiv \frac{1}{N_s}\sum_k \delta(E - \varepsilon_k)$ is the local density of states for the free electrons. Since the relevant frequency range for the self-energy is $|\omega| \sim \omega_0$, and

$\omega_0 \ll W$, where W is the bandwidth, we neglect the frequency dependence in the density of states, i.e. $N(\omega + \mu \pm \omega_0) \approx N(\mu) \approx N(\varepsilon_f)$, where ε_f is the Fermi energy. Furthermore, the strength of the electron-phonon coupling is given by the dimensionless parameter [7] $\lambda \equiv \frac{2N(\varepsilon_f)g^2}{\omega_0}$. Therefore, the imaginary part of the self-energy is expressed directly in terms of λ as

$$\Im m\Sigma(\omega) \;=\; -\frac{\pi\lambda\omega_0}{2}\sum_{\pm}\left[f^{\mp}(\omega \pm \omega_0) + n(\omega_0)\right]. \tag{SI-7}$$

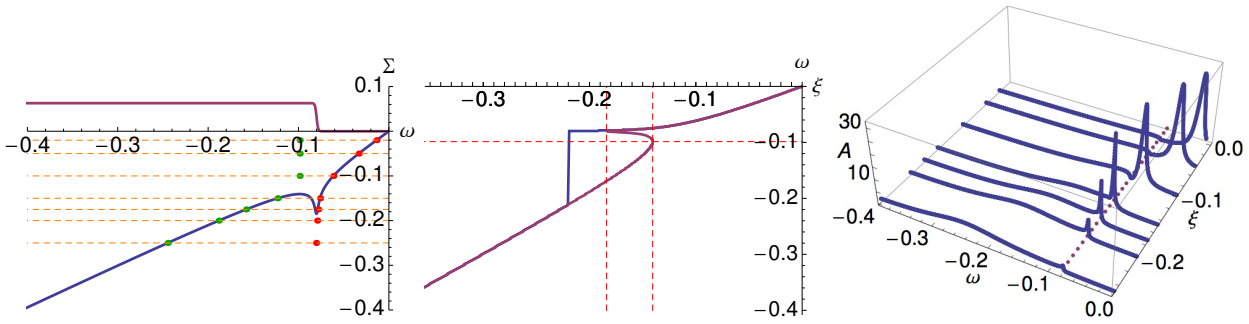

FIG. 2: Results for free electrons coupled to an Einstein phonon mode of frequency $\omega_0 = .08$ eV, with coupling strength $\lambda = 0.5$, at $T = 10$ K. **Right** panel: The EDCs at several representative momenta, the variable $\xi = v_f(k - k_F) = (1 + \lambda)V_L(k - k_F)$ here and in later figures. The dashed line indicates the phonon frequency, $\omega = -\omega_0$. Each EDC has two well-defined features, a peak followed by a hump (separated by a sharp dip for low momentum EDCs). **Middle** panel: The MDC dispersion (magenta) has no jump while the EDC dispersion (blue) shows a jump. The two vertical dashed lines partition momentum space into three regions. The horizontal dashed line indicates the location of the hump in the EDCs in the first (low-momentum) region. In the first two regions, the EDC dispersion follows the MDC dispersion (closest to zero frequency), while in the third (high momentum) region, it stays pinned to the phonon frequency over a large range of momentum, until it discontinuously jumps back down to the MDC dispersion. Note that $V_H = V_H^*$. **Left** panel: $\omega - \Re e\Sigma(\omega)$ and $-\Im m\Sigma(\omega)$ vs. ω. The horizontal dashed lines indicate the momenta associated with the corresponding EDCs in the right panel. The red dots indicate the locations of the peaks, and the green dots indicate the locations of the humps, as determined directly from each EDC.

We initially choose a typical intermediate strength value of $\lambda = 0.5$. We also add a small broadening $\eta = .01$ eV to the imaginary part of the self-energy. In Fig. (2), we display $\omega - \Re e\Sigma(\omega)$ and $-\Im m\Sigma(\omega)$ vs. ω (left panel), the EDC and MDC dispersions (middle panel), as well as the EDCs at several representative momenta (right panel) at $T = 10$ K. The EDC and MDC dispersions as well as the EDCs can be understood directly from the real and imaginary parts of the self-energy using Eq. (SI-5). From Eq. (SI-5), the the MDC at fixed ω is a Lorentzian of width $-\Im m\Sigma(\omega)$ and peak position $\xi^*(\omega) = \omega - \Re e\Sigma(\omega)$ [2]. Therefore, the MDC dispersion is obtained by inverting $\xi^*(\omega)$ to obtain $E(\xi)$. Since $\omega - \Re e\Sigma(\omega)$ is not

one-to-one, $E(\xi)$ is a multi-valued function.

To understand the EDC dispersion, we first examine the EDC curves in the right panel of Fig. (2). The momentum ξ associated with each curve is given by the location of the corresponding horizontal dashed line along the vertical axis in the left panel. The EDC at each momentum has two distinguishable features, a peak followed by a hump. In the left panel, the red and green dots indicate the location of the peak and hump, respectively, at each momentum, as determined directly from the EDC.

We partition the EDCs into three distinct momentum regions, $|\xi| < |\xi_1|$, $|\xi_1| < |\xi| < |\xi_2|$, and $|\xi| > |\xi_2|$, where the momenta ξ_1 and ξ_2 (the low-energy kink momentum) are denoted by the dashed vertical lines in the middle panel of Fig. (2). In the first region, $|\xi| < |\xi_1|$, the peak location, E_p^*, disperses according to the equation $\xi = E_p^* - \Re e\Sigma(E_p^*)$, while the hump location, E_h^*, remains at a fixed frequency, displayed by the horizontal dashed line in the middle panel. In addition, there is a sharp dip between the peak and the hump which is pinned to the phonon frequency, $-\omega_0$. Since $\Im m\Sigma(E_p^*)$ is constant throughout this region, the height of the peak does not change. On the other hand, since $|E_h^* - \xi - \Re e\Sigma(E_h^*)|$ decreases as $|\xi|$ is increased (and of course $\Im m\Sigma(E_h^*)$ is constant), the hump height grows as $|\xi|$ approaches $|\xi_1|$. Nevertheless, since the peak height remains greater than the hump height throughout this region (as will be shown below), the EDC dispersion is given by $E^* = E_p^*$.

In the second region, $|\xi_1| < |\xi| < |\xi_2|$, both E_p^* and E_h^* disperse according to the equation $\xi = E_{p,h}^* - \Re e\Sigma(E_{p,h}^*)$, E_p^* being the root closest to, and E_h^* being the root farthest from, zero frequency. Since $\Im m\Sigma(E_p^*)$ continues to remain constant and has the same value as in the first region, so does the height of the peak. Moreover, since $\Im m\Sigma(E_h^*)$ remains constant as well, the height of the hump remains the one which it reached at $\xi = \xi_1$. Finally, since $|\Im m\Sigma(E_h^*)| > |\Im m\Sigma(E_p^*)|$, the peak height is greater than the hump height, and therefore $E^* = E_p^*$.

In the third region, $|\xi| > |\xi_2|$, E_p^* is pinned to the phonon frequency $-\omega_0$, while E_h^* continues to disperse according to the equation $\xi = E_h^* - \Re e\Sigma(E_h^*)$. Since $\Im m\Sigma(E_h^*)$ continues to have the same value as in the second region, so does the height of the hump. Meanwhile, the peak height decreases, since $|E_p^* - \xi - \Re e\Sigma(E_p^*)|$ increases as $|\xi|$ is increased. Although initially $E^* = E_p^* = -\omega_0$, eventually, after $|\xi|$ has been sufficiently increased, the peak height falls below the hump height, and $E^* = E_h^*$. Accordingly, in the middle panel, we see that

in first two regions, the EDC dispersion follows the MDC dispersion, $E^* = E$ (closest to zero frequency). However, in the third region, E^* stays fixed at $-\omega_0$, until at sufficiently high momentum, it jumps back down to the MDC dispersion. Since the MDC and EDC dispersions coincide for large momentum, the velocities V_H and V_H^* are equal. We take these three features, a discontinuous jump in the EDC dispersion, a peak pinned to the phonon frequency in the EDC over a prolonged range of momentum, and the equality $V_H = V_H^*$, to be signatures of electron-Boson coupling in ARPES experiments. Similar calculations to the one above can be found in [2, 3], with analogous results.

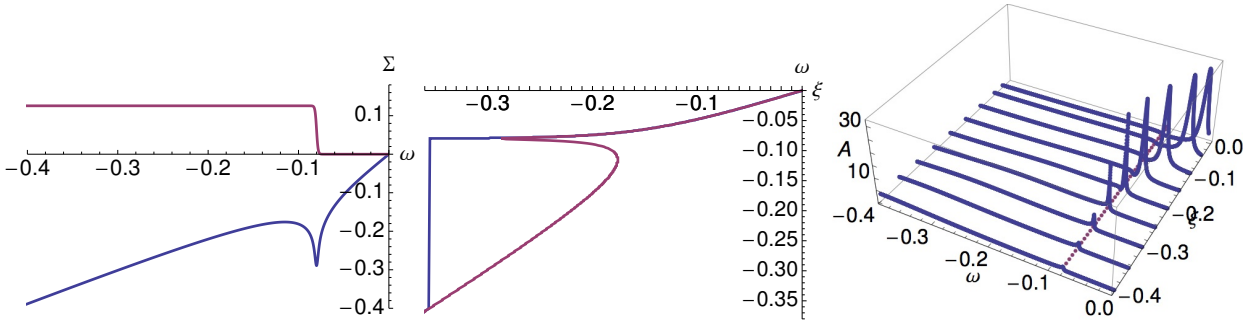

FIG. 3: To explore the effects of raising λ, we set $\lambda = 1$ while leaving all other parameters unchanged from Fig. (2). As a result, the kink momentum in the MDC dispersion becomes bigger, the hump in the EDCs is suppressed, the EDC dispersion stays pinned to the phonon frequency over a larger range of momentum, and the magnitude of the jump in the EDC dispersion grows.

To examine the effects of raising λ, we set $\lambda = 1$ leaving all other parameters unchanged, and plot the corresponding results in Fig. (3). This causes several noticeable changes to the results in Fig. (2). 1) The kink in the real part of the self-energy becomes sharper, which leads to a larger kink momentum, ξ_2, in the MDC dispersion. 2) $-\Im m\Sigma(E_h^*)$ becomes bigger, causing the height of the hump to go down. 3) As a direct consequence of 2), the range over which the EDC dispersion stays pinned to the phonon frequency becomes more prolonged in momentum space, and therefore the magnitude of the jump in the EDC dispersion also becomes bigger.

Setting $T \to 0$ in Eq. (SI-7), and plugging it into Eq. (SI-6), we find that to linear order in $\omega \ll \omega_0$, $\Re e\Sigma(\omega) = -\lambda\,\omega$. Therefore, $\lambda = \frac{v_f}{V_L} - 1$ (see also [8]). According to the normal state data ($T = 115$ K) from [4, 9, 10] (since $T \ll \omega_0$, this zero temperature formula still applies), $V_L = 1.47\text{eV}\,\mathring{A}$ and $v_f = 2.7\text{eV}\,\mathring{A}$, yielding $\lambda = 0.84$. In principle, one might argue for the

larger value of $v_f \sim 5.4$ eV $\mathring{A}$ from the ARPES observed width of the band [17], leading to $\lambda \sim 2.67$, a very high value indeed. However, we will assume, with several authors of the Boson-coupling models, that the smaller estimate is overall more reasonable. Using these experimentally relevant values, in Fig. (4), we plot $\omega - \Re e\Sigma(\omega)$ and $-\Im m\Sigma(\omega)$ vs. ω (left panel), as well as the MDC and EDC dispersions (middle panel), and the EDCs at several representative momenta (right panel). Due to the higher value of T, the self-energy curves have been rounded out somewhat as compared to Fig. (2), but retain the same features. We see that the EDC dispersion once again follows the MDC dispersion (closest to zero frequency) in the first two momentum regions, until it (nearly) flattens out in the third region, where the peak is pinned to the phonon frequency, $-\omega_0$, in the corresponding EDCs. As the momentum is increased such that the height of this peak shrinks below the height of the hump, the EDC dispersion jumps discontinuously down from the phonon frequency, to the MDC dispersion. Consequently, we see that the velocities of the MDC and EDC dispersion coincide above the kink; i.e. $V_H = V_H^*$.

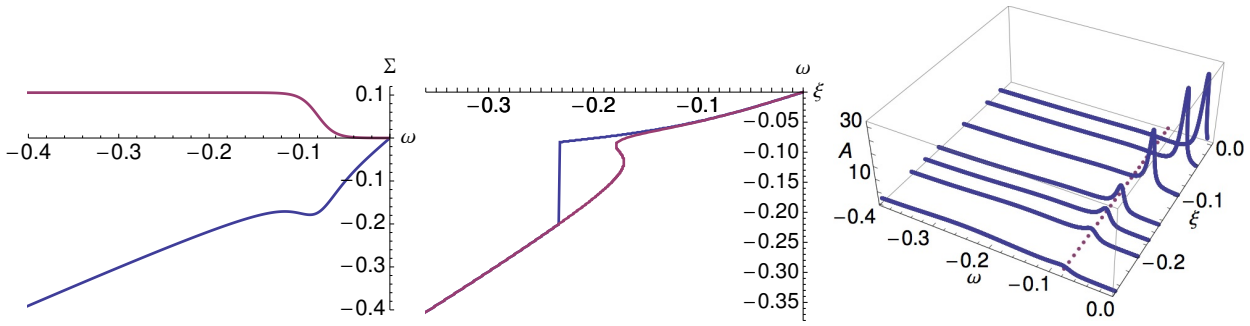

FIG. 4: We now use the experimentally relevant values of $\lambda = 0.84$ and $T = 115$ K. The curves retain the same qualitative features as in Fig. (2), which are less sharp in the present case due to the higher value of T.

We now examine how these results are affected by retaining the full frequency-dependence of the density of states in Eq. (SI-6). Just as was done in [4], we use the dispersion tb2 from [10]. In this case, $\varepsilon_f = 0$ and $N(\varepsilon_f) = 0.61$ eV^{-1}. Retaining the same values of $T = 115$ K and $\lambda = 0.84$, we set $g = 0.23$ eV in Eq. (SI-6). We also set $\mu \approx \varepsilon_f = 0$. In Fig. (5), we plot $\omega - \Re e\Sigma(\omega)$ and $-\Im m\Sigma(\omega)$ vs. ω (left panel), as well as the MDC and EDC dispersions (middle panel), and the EDCs at several representative momenta (right panel). Due to the functional form of the density of states (see the inset of the left panel), the MDC

dispersion acquires two additional branches which yield large frequency values. In the first two momentum regions (below the low-energy kink momentum), the EDC dispersion follows the lowest-frequency branch of the MDC dispersion. As the momentum increases into the third region (above the low-energy kink momentum), the peak stays pinned to the phonon frequency in the corresponding EDCs. Moreover, since $|\Im m\Sigma\left(E(\xi)\right)| \gg |\Im m\Sigma(-\omega_0)|$, where $E(\xi)$ can be any branch of the MDC dispersion, the EDC dispersion stays pinned to the phonon frequency as well. As the momentum is increased further and the height of the peak decreases sufficiently, the EDC dispersion jumps discontinuously onto the highest-frequency branch of the MDC dispersion, since this is the one with the smallest value of $|\Im m\Sigma\left(E(\xi)\right)|$, and hence $V_H = V_H^*$. This small value of $|\Im m\Sigma\left(E(\xi)\right)|$ leads to a noticeable hump at high-frequencies in the corresponding EDCs.

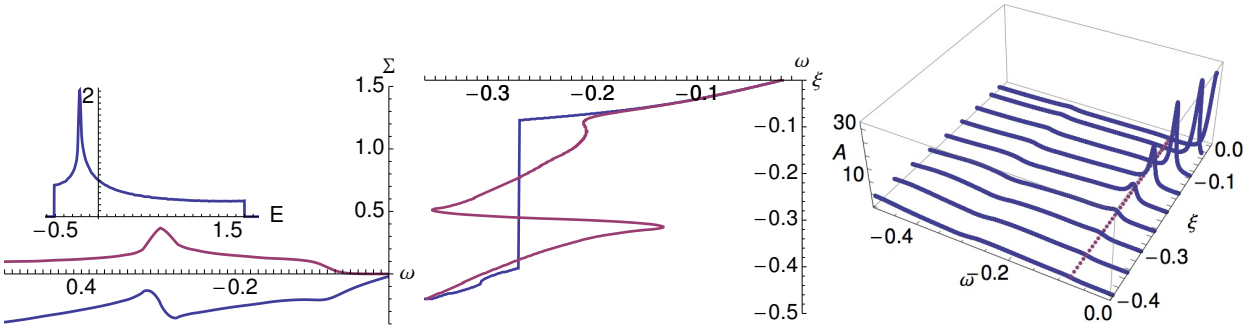

FIG. 5: We explore the effects of using the full frequency-dependence of the density of states in Eq. (SI-6), with $\lambda = 0.84$ and $T = 115$ K. Due to the functional form of the density of states (displayed as an inset in the left panel), the MDC dispersion acquires two additional branches which yield large frequency values. Below the low-energy kink momentum, the EDC dispersion follows the lowest-frequency branch of the MDC dispersion. Above the low-energy kink momentum, the EDC dispersion initially stays pinned to the phonon frequency, until it discontinuously jumps onto the highest-frequency branch of the MDC dispersion ($V_H = V_H^*$). A noticeable hump also develops at high-frequencies, in the corresponding EDCs.

Thus far, we have considered only free electrons coupled to a Boson mode. We now include electron-electron correlations. Following [11], we assume that

$$\Im m\Sigma_{el-el}(\omega) = -\frac{(\tau^2+\omega^2)}{\Omega_0}\exp\left[\frac{-(\tau^2+\omega^2)}{\nu_0^2}\right] - \eta, \tag{SI-8}$$

where $\Sigma_{el-el}(\omega)$ is the self-energy due only to electron-electron correlations, $\tau \equiv \pi k_B T$, $T = 115$ K, $\Omega_0 = .14$ eV, $\nu_0 = .5$ eV, and we set $\eta = .01$ eV. This phenomenological form for $\Im m\Sigma_{el-el}(\omega)$ reproduces the correct Fermi-liquid behavior at low frequencies, and extrapolates to high frequencies in a reasonable way. Furthermore, we assume a flat band for ε_k of bandwidth W, i.e $N(E) = \frac{1}{W}\Theta(\frac{W}{2} - |E|)$, and set $\mu \approx \varepsilon_f = 0$. Retaining the same values of $N(\varepsilon_f) = 0.61$ eV^{-1} and $\lambda = 0.84$ as before, yields the values $W = 1.64$ eV and $g = 0.23$ eV. The self-energy is now given by the sum $\Sigma(\omega) = \Sigma_{el-el}(\omega) + \Sigma_{el-ph}(\omega)$, where the imaginary part of the latter term is

$$\begin{aligned} \Im m\Sigma_{\text{el-ph}}(\omega) \;=\; & -\pi g^2 \sum_{\pm} A_{\text{el-el,loc}}(\omega \pm \omega_0) \times \\ & \left[f^{\mp}(\omega \pm \omega_0) + n(\omega_0) \right], \end{aligned} \tag{SI-9}$$

while the real part is as usual given by applying the Hilbert transform to Eq. (SI-9). Here, $A_{\text{el-el,loc}}(\omega) = \frac{1}{N_s}\sum_k A_{\text{el-el}}(\vec{k},\omega)$, where $A_{\text{el-el}}(\vec{k},\omega)$ is given by Eq. (SI-5) with the substitution $\Sigma(\omega) \to \Sigma_{\text{el-el}}(\omega)$. Eq. (SI-5) continues to express $A(\vec{k},\omega)$ in terms of $\Sigma(\vec{k},\omega)$, where both objects now include electron-electron and electron-phonon correlations.

In Fig. (6), we plot $\omega - \Re e\Sigma(\omega)$ and $-\Im m\Sigma(\omega)$ vs. ω (left panel), as well as the MDC and EDC dispersions (middle panel), and the EDCs at several representative momenta (right panel), from this calculation. Due to the specific form of the self-energy, $\Sigma_{el-el}(\omega)$ (both $-\Im m\Sigma_{el-el}(\omega)$ and $A_{\text{el-el,loc}}(\omega)$ are displayed as an inset in the left panel), the highest-frequency branch of the MDC dispersion yields very large values of the frequency. Just as in the cases considered above, for momentum $|\xi|$ below the low-energy kink momentum, the EDC dispersion follows the lowest-frequency branch of the MDC dispersion, $E_l(\xi)$. As the momentum $|\xi|$ is increased above the low-energy kink momentum, the rapid increase in $|\Im m\Sigma\left(E_l(\xi)\right)|$ causes the peak in the EDC as well as the EDC dispersion to stay pinned to the phonon frequency. As the momentum is increased further, $|\Im m\Sigma\left(E_h(\xi)\right)|$ becomes comparable to $|\Im m\Sigma(-\omega_0)|$, where $E_h(\xi)$ is the highest-frequency branch of the MDC dispersion. At this point, the EDC dispersion jumps discontinuously from the phonon frequency onto the highest-frequency branch of the MDC dispersion, and hence $V_H = V_H^*$. This is also reflected in the corresponding EDCs, which acquire a hump at high-frequencies.

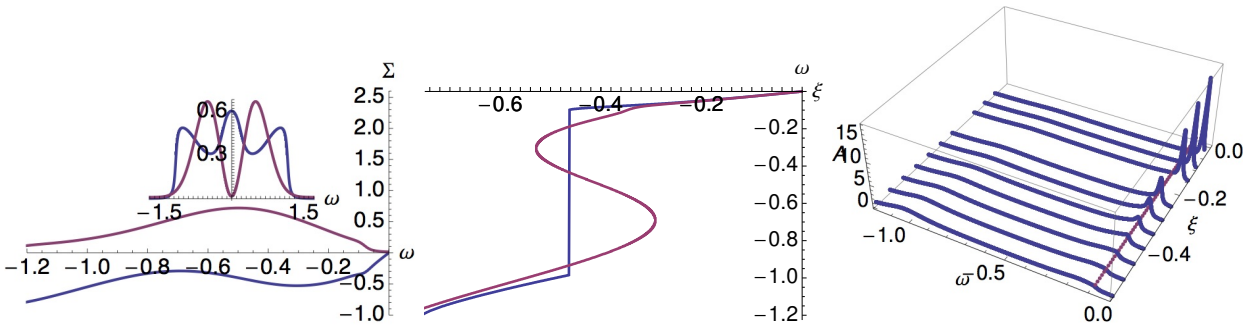

FIG. 6: We explore the effects of Fermi-liquid-like electron-electron correlations (Eq. (SI-8)), with $\lambda = 0.84$ and $T = 115$ K. Due to the functional form of the self-energy, $\Sigma_{el-el}(\omega)$ (both $-\Im m\Sigma_{el-el}(\omega)$ and $A_{\text{el-el,loc}}(\omega)$ are displayed as an inset in the left panel), the highest-frequency branch of the MDC dispersion yields very large values of the frequency. Below the low-energy kink momentum, the EDC dispersion follows the lowest-frequency branch of the MDC dispersion. Above the low-energy kink momentum, the EDC dispersion initially stays pinned to the phonon frequency, until it discontinuously jumps onto the highest-frequency branch of the MDC dispersion ($V_H = V_H^*$). This is also reflected in the corresponding EDCs, which acquire a hump at high-frequencies.

In conclusion, we find that in all of the above cases of electrons interacting with a Boson mode, the EDCs are characterized by three signatures: (1) a peak pinned to the Boson-frequency over a large range of momentum, (2) the EDC dispersion jumps discontinuously from the Boson-frequency onto (the highest-frequency branch of) the MDC dispersion, and (3) $V_H = V_H^*$. These three features are jointly present for most parameters explored, and may be viewed as the signatures of kinks produced by this mechanism.

(III) EXTREMELY CORRELATED FERMI LIQUID THEORY OF KINKS

In this section we present the theoretical details of the ECFL calculation of kinks. We first show the results of a low energy and momentum expansion of the ECFL Greens function in terms of a few parameters. Earlier studies [12–14] show that the two self energies Φ, Ψ of the ECFL theory are to a large extent similar to the self energies of a standard intermediate coupling Fermi liquid, and yet due to their specific combination that occurs in Eq. (SI-10) and Eq. (SI-12) end up providing a non trivial resulting theory. Indeed in Ref. (12) a similar

low energy expansion in high dimensions, was tested successfully against the numerical results of the Dynamical Mean Field Theory (DMFT). It should be noted that the DMFT theory is designed for high dimensions, where the momentum dependence of the Dyson self energy and Ψ self energy of the ECFL theory drops out. In this section we allow for momentum dependence of both self energies in the ECFL formalism, this is in-fact the only distinction between the present expansion and that in Ref. (12). We see below that this momentum dependence is essential for describing the low energy kinks in the occupied part of the ARPES spectrum.

Low energy expansion of the ECFL theory

We start with the ECFL Greens function $\mathcal{G}$ expressed in terms of the auxiliary Greens function $\mathbf{g}$ and the caparison function $\widetilde{\mu}$ Ref. (15) and Ref. (16), we write

$$\mathcal{G}(\vec{k}, i\omega) = \mathbf{g}(\vec{k}, i\omega) \times \widetilde{\mu}(\vec{k}, i\omega), \tag{SI-10}$$

and with the latter expressed in terms of the two self energies $\Phi(\vec{k}, i\omega_n), \Psi(\vec{k}, i\omega_n)$ as:

$$\widetilde{\mu}(\vec{k}, i\omega_n) = 1 - \frac{n}{2} + \Psi(\vec{k}, i\omega_n) \tag{SI-11}$$

$$\mathbf{g}^{-1}(\vec{k}, i\omega_n) = i\omega_n + \boldsymbol{\mu} - (1 - \frac{n}{2})\varepsilon_k - \Phi(\vec{k}, i\omega_n), \tag{SI-12}$$

where n is the electron number per site, $\omega_n = (2n+1)\pi/\beta$ the Matsubara frequency, which we analytically continue $i\omega \to \omega + i0^+$. Let us define $\hat{k}$ as the *normal deviation* from the Fermi surface i.e. $\hat{k} = (\vec{k} - \vec{k}_F).\vec{\nabla}\varepsilon_{k_F}/|\vec{\nabla}\varepsilon_{k_F}|$. Our first objective is to Taylor expand these equations for small ω and $\hat{k}$, as explained above. We carry out a low frequency expansion as follows:

$$1 - \frac{n}{2} + \Psi(\vec{k}, \omega) = \alpha_0 + c_\Psi(\omega + \nu_\Psi\ \hat{k}\, v_f) + i\mathcal{R}/\gamma_\Psi + \mathcal{O}(\omega^3), \tag{SI-13}$$

where the frequently occurring Fermi liquid function $\mathcal{R} = \pi\{\omega^2 + (\pi k_B T)^2\}$, $v_f = (\partial_k \varepsilon_k)_{k_F}$ is the *bare* Fermi velocity, and the four parameters $\alpha_0, c_\Psi, \nu_\Psi, \gamma_\Psi$ are coefficients in the Taylor expansion having suitable dimensions. Similarly we expand the auxiliary Greens function

$$\mathbf{g}^{-1}(k, \omega) = (1 + c_\Phi)\left(\omega - \nu_\Phi\ \hat{k}\, v_f + i\mathcal{R}/\Omega_\Phi + \mathcal{O}(\omega^3)\right), \tag{SI-14}$$

where we have added another three coefficients in the Taylor expansion $c_\Phi, \nu_\Phi, \Omega_\Phi$.

To carry out this reduction we first trade the two parameters c_Ψ, γ_Ψ in favor of parameters Ω_Ψ and s by defining $c_\Psi = \frac{\alpha_0}{\Omega_\Psi}$ and $\gamma_\Psi = \frac{s\Omega_\Phi}{c_\Psi}$, where the dimensionless parameter $0 \leq s \leq 1$. With these expansions and the quasiparticle weight determined in terms of the expansion parameters as $Z = \frac{\alpha_0}{1+c_\Phi}$, we find

$$\mathcal{G} = \frac{Z}{\Omega_\Psi} \frac{\Omega_\Psi + \omega + \nu_\Psi\ \hat{k}\, v_f + i\mathcal{R}/(s\Omega_\Phi)}{\omega - \nu_\Phi\ \hat{k}\, v_f + i\mathcal{R}/\Omega_\Phi}. \tag{SI-15}$$

Using $A(\hat{k}, \omega) = -\frac{1}{\pi}\Im m\, \mathcal{G}$ we find the spectral function

$$A(\hat{k}, \omega) \ = \ \frac{Z}{\pi} \frac{\frac{\mathcal{R}}{\Omega_\Phi}}{(\omega - \nu_\Phi\ \hat{k}\, v_f)^2 + (\frac{\mathcal{R}}{\Omega_\Phi})^2} \times \widetilde{\mu}_c(\hat{k}, \omega) \tag{SI-16}$$

Here the caparison *factor*, (not to be confused with the caparison *function* in Eq. (SI-10)), is found as

$$\begin{aligned} \widetilde{\mu}_c(\hat{k}, \omega) \ &= \ 1 - \xi(\hat{k}, \omega) \\ \xi(\hat{k}, \omega) \ &= \ \frac{1}{\Delta_0}(\omega - \nu_0\ \hat{k}\, v_f) \end{aligned} \tag{SI-17}$$

In Eq. (SI-17) we have introduced two composite parameters

$$\Delta_0 = \frac{s}{1-s}\Omega_\Psi, \quad \text{and} \quad \nu_0 = \frac{1}{1-s}\nu_\Phi + \frac{s}{1-s}\nu_\Psi. \tag{SI-18}$$

This procedure eliminates the *three* old parameters s, Ω_Ψ and ν_Ψ in favor of the *two* emergent energy scale Δ_0 and velocity ν_0.

It is interesting to count the reduction in the number of free parameters from the starting value of seven in Eq. (SI-13) and Eq. (SI-14). Already in Eq. (SI-15) we have a reduction to six, since the quasiparticle weight Z combines two of the original parameters. Since Eq. (SI-18) subsumes three parameters into two, the spectral function in Eq. (SI-16) contains only five parameters: the two velocities $\nu_0\, v_f, \nu_\Phi\, v_f$, and the two energies Ω_Φ, Δ_0, in addition to the overall scale factor Z.

We will see below that the parameters that are measurable from energy dispersions are best expressed in terms of certain combinations of the velocities. In order to make the connection with the experiments close, we will redefine the two velocities in terms of an

important dispersion velocity at the lowest energies V_L and a dimensionless ratio r, on using the definitions:

$$\begin{aligned} \nu_\Phi \, v_f &= V_L \\ \nu_0 \, v_f &= r \times V_L. \end{aligned} \tag{SI-19}$$

In order to account for the difference between laser ARPES and synchrotron AREPS having different incident photon energies, we will make two phenomenological modifications in Eq. (SI-16) following Ref. (17)

$$\mathcal{R}(\omega)/\Omega_\Phi \to \mathcal{R}(0)/\Omega_\Phi = \pi\{\pi k_B T\}^2/\Omega_\Phi + \eta \equiv \Gamma_0 \tag{SI-20}$$

where η represents an elastic energy from impurity scattering, dependent upon the energy of the incident photon in the ARPES experiments. In the spirit of a low energy expansion $\mathcal{R}$ is evaluated at $\omega = 0$. Thus Γ_0 is a T dependent constant, which subsumes the two parameters η and Ω_Φ, and thus the total parameter count is still five. Secondly for extension to higher energies, we "renormalize" the parameter ξ in Eq. (SI-17) according to a recently discussed prescription following from a theoretical calculation Ref. (18) as $\widetilde{\mu}_c \to \{1 - \frac{\xi}{\sqrt{1+c_a\xi^2}}\}$, where $c_a \sim 5.4$ near optimum doping $\delta \sim 0.15$ as estimated recently. This correction ensures that the caparison factor exhibits the correct linear behavior for small ξ, and remains positive definite at high energies. Thus we write the spectral function in terms of the new variables as

$$A(\vec{k},\omega) = \frac{Z}{\pi} \frac{\Gamma_0}{(\omega - V_L \, \hat{k})^2 + \Gamma_0^2} \times \{1 - \frac{\xi}{\sqrt{1 + c_a \xi^2}}\}, \tag{SI-21}$$

with $\xi = \frac{1}{\Delta_0}(\omega - r \, V_L \, \hat{k})$. We should keep in mind that these expressions follow from a low energy expansion, and is limited to small $\hat{k}$ and ω, so that the dimensionless variable $|\xi|_{max} \sim \mathcal{O}(1)$. Microscopic calculations of all these parameters is possible in the ECFL theory. One important parameter is the energy scale Δ_0 which is found to be much reduced from the band width, due to extremely strong correlations. A related energy is the effective Fermi liquid temperature scale where the T^2 dependence of the resistivity gives way to a linear dependence. This scale is estimated in the limit of large dimensions from Ref. (18) to be as low as 45 K near optimum doping, i.e. much reduced from naive expectations.

For the present purposes we take a different track, we note that the ARPES fits are overdetermined, so that we can determine the few parameters of the low energy theory from a fairly small subset of measurements. The five final (composite) parameters defining the spectral function Eq. (SI-21) are $Z, V_L, r, \Delta_0, \Gamma_0$, where $c_a \sim 5.4$. Of these Z is multiplicative, it is only needed for getting the absolute scale of the spectral function, and c_a does not play a significant role near zero energy, it is required only at high energies. Thus the spectra relevant to EDC and MDC will require only *four* parameters $V_L, r, \Delta_0, \Gamma_0$. These suffice to determine the low energy theory and thus to make a large number of predictions; i.e. implying non trivial relationships amongst observables. Many of the predictions rely only on the overall structure of the theory and not its details.

The EDC and MDC dispersion relations and kinks

Starting from Eq. (SI-21), we can compute the energy dispersions for MDC (varying $\hat{k}$ while keeping ω fixed) and the EDC spectra (varying ω while keeping $\hat{k}$ fixed). In terms of a momentum type variable

$$Q(\hat{k}) = \Delta_0 + (r-1)\hat{k}\, V_L \tag{SI-22}$$

we can locate the peaks of Eq. (SI-21) using elementary calculus since c_a only plays a role at high energies, we set $c_a \to 0$ when performing the extremization and find the MDC dispersion

$$E(k) \;=\; \frac{1}{2-r}\left(\hat{k}\, V_L + \Delta_0 - \sqrt{r(2-r)\,\Gamma_0^2 + Q^2}\right), \tag{SI-23}$$

and the EDC dispersion

$$E^*(k) \;=\; \left(r\;\hat{k}\, V_L + \Delta_0 - \sqrt{\Gamma_0^2 + Q^2}\right). \tag{SI-24}$$

Using these two dispersions and expanding them in different regimes, we can extract all the parameters of the kinks.

Kink momentum

As explained in the main paper, when we set $T = 0 = \eta$ so that $\Gamma_0 = 0$, both the EDC and MDC dispersions contain an ideal kink at the kink momentum. Therefore, using Eqs.

(SI-23) and (SI-24), the condition $Q = 0$ locates the kink momentum for both dispersions:

$$\hat{k}_{kink} = \frac{\Delta_0}{(1-r)V_L}, \tag{SI-25}$$

it corresponds to occupied momenta, i.e. $\hat{k}_{kink} v_f < 0$, provided that $r > 1$. We thus can express $\Delta_0 = \hat{k}_{kink}\, V_L(1-r)$, enabling us to usefully rewrite

$$Q = (r-1)\, V_L\, (\hat{k} - \hat{k}_{kink}) = \Delta_0 \{1 - \frac{\hat{k}}{\hat{k}_{kink}}\}. \tag{SI-26}$$

As required by the ideal kink, Q changes sign at the kink momentum,

$$\text{sign}(Q) = \text{sign}(\hat{k} - \hat{k}_{kink}). \tag{SI-27}$$

Ideal Kink energies: T=0

Using Eq. (SI-23) and Eq. (SI-24), in conjunction with Eq. (SI-25), the ideal kink energy is the same for both dispersions, and is given by

$$E_{kink}^{ideal} = -\frac{1}{r-1}\Delta_0. \tag{SI-28}$$

We can also usefully estimate this ideal kink energy from the asymptotic velocities in the far zone, as explained in the main paper.

The non-ideal i.e. $T > 0$ kink energy

The EDC and MDC kink energies for the non-ideal case can be viewed in a couple of ways. We have argued in the main paper that these are best defined by fixing the momentum $\hat{k} = \hat{k}_{kink}$ and reading off the energy at this value. This is an unambiguous method independent of the detailed shape of the kink, since it only requires knowledge of $\hat{k}_{kink}$, which can be found from an asymptotic measurement as we have argued in the main paper. We can put $Q = 0$ and $\hat{k} \to \hat{k}_{kink}$ in Eq. (SI-24) and Eq. (SI-23) and read off the kink energies:

$$E_{kink}^{EDC} = E_{kink}^{ideal} - \Gamma_0, \tag{SI-29}$$

$$E_{kink}^{MDC} = E_{kink}^{ideal} - \Gamma_0\sqrt{\frac{r}{2-r}}. \tag{SI-30}$$

We observe that the MDC kink energy is real provided $2 \geq r \geq 1$. Note also that at $T = 0$ and $\eta = 0$, the two energies both reduce to the ideal kink energy.

The ideal energy dispersions

At $T = 0$ or for $|Q| \gg \Gamma_0$, the two dispersions Eq. (SI-24) and Eq. (SI-23) become:

$$E^*(k) \sim \left[r - (r-1)\,\mathrm{sign}(\hat{k} - \hat{k}_{kink})\right] \hat{k}\, V_L \;+\; 2\Delta_0 \Theta(\hat{k}_{kink} - \hat{k}) \tag{SI-31}$$

and

$$E(k) \sim \frac{1}{2-r}\left[1 - (r-1)\,\mathrm{sign}(\hat{k} - \hat{k}_{kink})\right] \hat{k}\, V_L \;+\; \frac{2\Delta_0}{2-r}\Theta(\hat{k}_{kink} - \hat{k}). \tag{SI-32}$$

The velocities in the asymptotic regime $|\hat{k}| \gg \hat{k}_{kink}$ can be found from the slopes of these, and are therefore temperature-independent. For $\hat{k} \gg \hat{k}_{kink}$ we get the "low" velocities

$$\begin{aligned} \frac{dE(k)}{d\hat{k}} &= V_L \\ \frac{dE^*(k)}{d\hat{k}} &= V_L^* = V_L \end{aligned} \tag{SI-33}$$

and thus the EDC and MDC velocities are identical. For $\hat{k} \ll \hat{k}_{kink}$ we get the "high" velocities

$$V_H = \frac{dE(k)}{d\hat{k}} = \frac{r}{2-r} V_L, \tag{SI-34}$$

$$V_H^* = \frac{dE^*(k)}{d\hat{k}} = (2r-1) V_L. \tag{SI-35}$$

We may cast Eq. (SI-35) into an interesting form

$$V_H^* = \left\{\frac{3V_H - V_L}{V_H + V_L}\right\} V_L, \tag{SI-36}$$

it is significant since the EDC spectrum velocity is exactly determined in terms of the two MDC spectrum velocities. It is also a testable result, we show elsewhere in the paper how this compares with known data. Note that the four independent parameters $V_L, r, \Delta_0, \Gamma_0$ alluded to in the discussion below Eq. (SI-21), can be determined from the directly measurable parameters $V_L, V_H, \hat{k}_{kink}, \Gamma_0$ (SI-34,SI-25,SI-3). Therefore, either set of parameters gives complete knowledge of the EDC and MDC dispersions, as well as the spectral function (up to an overall scale).

Near Zone: Corrections to Energy dispersion due to finite T.

In the regime dominated by finite T and effects of η the elastic scattering parameter, we can also perform an expansion in the limit when $|Q| \ll \Gamma_0$, using Eq. (SI-23) and Eq. (SI-24). The the first few terms are

$$\begin{aligned} E(k) &= \frac{\Delta_0}{1-r} - \sqrt{\frac{r}{2-r}}\,\Gamma_0 + \frac{V_L}{2-r}(\hat{k} - \hat{k}_{kink}) \\ &\quad - \frac{(1-r)^2}{2\sqrt{r(2-r)^3}}\,\frac{V_L^2}{\Gamma_0}(\hat{k} - \hat{k}_{kink})^2 + \dots \end{aligned} \tag{SI-37}$$

Similarly for the EDC dispersion

$$\begin{aligned} E^*(k) &= \frac{\Delta_0}{1-r} - \Gamma_0 + rV_L(\hat{k} - \hat{k}_{kink}) \\ &\quad - \frac{(1-r)^2}{2}\,\frac{V_L^2}{\Gamma_0}(\hat{k} - \hat{k}_{kink})^2 + \dots \end{aligned} \tag{SI-38}$$

These formulas display a shift in the energies due to Γ_0 and also a Γ_0 dependent curvature. Since the regime of this expansion, $|Q| < \Gamma_0$ is different from that of the expansion in Eq. (SI-35) and Eq. (SI-33), we note that velocities are different as well. Thus one must be careful about specifying the regime for using the velocity formulae.

Let us note that in this regime $|Q| < \Gamma_0$ the two dispersions differ, with the EDC higher.

$$\begin{aligned} E^*(k) - E(k) &= \{\sqrt{\frac{r}{2-r}} - 1\}\Gamma_0 \\ &\quad - \frac{(1-r)^2}{2-r}V_L(\hat{k} - \hat{k}_{kink}) + \dots \end{aligned} \tag{SI-39}$$

This equation gives a prescription for estimating Γ_0 in cases where the other parameters are known. Alternatively in the MDC dispersion we expect to see a curvature only near the location of the kink, this is sufficient to fix Γ_0: from Eq. (SI-37)

$$\frac{d^2E(k)}{d\hat{k}^2} = -\frac{(r-1)^2}{\sqrt{r(2-r)^3}}\,\frac{V_L^2}{\Gamma_0}. \tag{SI-40}$$

The curvature $\frac{d^2E(k)}{d\hat{k}^2}$ can be estimated from the experimental data to provide an estimate of Γ_0.

The Dyson self energy

For completeness we present the low energy expansion of the Dyson self energy, which gives rise to the spectral function in Eq. (SI-21). We may define the Dyson self energy from

$$\Sigma_D \;=\; \omega + \boldsymbol{\mu} - \varepsilon_k - \mathcal{G}^{-1} \tag{SI-41}$$

Using Eq. (SI-15) we obtain

$$\Im m\, \Sigma_D = -\frac{1}{Z}\frac{\mathcal{R}}{\Omega_\Phi}\frac{1-\frac{1}{\Delta_0}(\omega-\nu_0\ \hat{k}\, v_f)}{\{1+(\omega+\nu_\Psi\ \hat{k}\, v_f)/\Omega_\Psi\}^2+\frac{\mathcal{R}^2}{s^2\Omega_\Phi^2\Omega_\Psi^2}} \tag{SI-42}$$

The corresponding real part is given by

$$\begin{aligned}
\Re e\, \Sigma_D \;&=\; \boldsymbol{\mu} - \boldsymbol{\mu}_0 + \omega - \ \hat{k}\, v_f \\
&\quad -\frac{1}{Z}\frac{(\omega-\nu_\Phi\ \hat{k}\, v_f)+\frac{1}{\Omega_\Psi}q_2}{\{1+(\omega+\nu_\Psi\ \hat{k}\, v_f)/\Omega_\Psi\}^2+\frac{\mathcal{R}^2}{s^2\Omega_\Phi^2\Omega_\Psi^2}} \\
q_2 \;&=\; (\omega+\nu_\Psi\ \hat{k}\, v_f)(\omega-\nu_\Phi\ \hat{k}\, v_f)+\frac{\mathcal{R}^2}{s\Omega_\Phi^2}.
\end{aligned} \tag{SI-43}$$

The q_2 term is quadratic (or higher) in the small variables $\omega,\ \hat{k}\, v_f$, however these small terms are needed if we want to reproduce exactly Eq. (SI-16).

Useful identities and some Fermi Liquid parameters.

We list a few useful identities relating the various parameters

$$\begin{aligned}
\Omega_\Psi \;&=\; \frac{1-s}{s}\,\Delta_0, \\
s \;&=\; \frac{\Delta_0}{\Delta_0+\Omega_\Psi} \\
\nu_0 \;&=\; \frac{\nu_\Phi + s\,\nu_\Psi}{1-s} = r\,\nu_\Phi \\
\nu_\Psi \;&=\; \frac{r-1-rs}{s}\,\nu_\Phi \\
r-1 \;&=\; \frac{\Delta_0}{\Omega_\Psi}\left(1+\frac{\nu_\Psi}{\nu_\Phi}\right)
\end{aligned} \tag{SI-44}$$

Let us note the Fermi liquid renormalizations from Eq. (SI-41)

$$\begin{aligned} \left.\frac{d\Sigma_D}{d\hat{k}}\right|_{FS} &= (\frac{V_L}{Z} - v_f) \\ \left.\frac{d\Sigma_D}{d\omega}\right|_{FS} &= (1 - \frac{1}{Z}) \end{aligned} \tag{SI-45}$$

Therefore we write the Fermi liquid mass enhancement that determines the heat capacity as:

$$\frac{m}{m^*} = Z\left\{1 + \frac{1}{v_f}\left.\frac{d\Sigma_D}{d\hat{k}}\right|_{FS}\right\} = V_L/v_f = \nu_\Phi. \tag{SI-46}$$

Thus ν_Φ is the inverse mass enhancement factor, obtainable from the ratio of the heat capacity and the bare density of states. In this model we note that ν_Φ is not obliged to vanish as Z near the half filled limit $n \to 1$, but may be a finite number of $O(1)$. This is unlike the Brinkman Rice "heavy metal' type behavior $m/m^* \propto Z$, which is prototypical of theories with a momentum independent self energy.

Finally we note that the condition for the kink to occur is, we recall, $r > 1$. From Eq. (SI-44) we see that this requires a finite Ω_Ψ (so that $1 > s > 0$). We also need $\Delta_0 > 0$ and $\left(1 + \frac{\nu_\Psi}{\nu_\Phi}\right) > 0$.

[SI-1] Yang, K., *et al.* Normal-state electronic structure in the heavily overdoped regime of Bi1.74 Pb0.38 Sr1.88 Cu $O_{6+\delta}$ single-layer cuprate superconductors: An angle-resolved photoemission study. *Physical Review B* **73**.14 (2006): 144507.

[SI-2] Cuk, T., *et al.* A review of electron-phonon coupling seen in the high-Tc superconductors by angle-resolved photoemission studies (ARPES). *Physica Status Solidi (b)* **242**, 1129 (2005).

[SI-3] He, J. *et. al.*, Coexistence of Two Sharp-Mode Couplings and their Unusual Momentum Dependence in the Superconducting State of Bi2 Sr2 CaCu2 $O_{8+\delta}$ Revealed by Laser-Based Angle-Resolved Photoemission. *Physical Review Letters* **111**.10 (2013): 107005.

[SI-4] S. Vig *et. al.*, Fluctuating charge order in the optimally doped high temperature superconductor Bi2Sr2CaCu2O_{8+x}, arXiv:1509.04230 (2015).

[SI-5] Migdal, A. B. Interaction between electrons and lattice vibrations in a normal metal. *Sov. Phys. JETP* **7**.6 (1958): 996-1001.

[SI-6] Engelsberg, S. and J. R. Schrieffer. Coupled electron-phonon system. *Physical Review* **131**.3 (1963): 993.

[SI-7] Gunnarsson, O., V. Meden, and K. Schnhammer. Corrections to Migdals theorem for spectral functions: A cumulant treatment of the time-dependent Greens function. *Physical Review B* **50**.15 (1994): 10462.

[SI-8] Chubukov, A. V., and M. R. Norman. Dispersion anomalies in cuprate superconductors. *Physical Review B* **70**.17 (2004): 174505.

[SI-9] Kaminski, A., *et al.* Renormalization of spectral line shape and dispersion below Tc in Bi2 Sr2 CaCu2 $O_{8+\delta}$. *Physical Review Letters* **86**.6 (2001): 1070.

[SI-10] Norman, M. R. Linear response theory and the universal nature of the magnetic excitation spectrum of the cuprates. *Physical Review B* **75**.18 (2007): 184514.

[SI-11] Shastry, B. Sriram. Anatomy of the self-energy. *Physical Review B* **84**.16 (2011): 165112.

[SI-12] Žitko, R., *et al.* Extremely correlated Fermi liquid theory meets dynamical mean-field theory: Analytical insights into the doping-driven Mott transition. *Physical Review B* **88**.23 (2013): 235132.

[SI-13] Shastry, B. Sriram, Edward Perepelitsky, and Alex C. Hewson. Extremely correlated Fermi liquid study of the U= ∞ Anderson impurity model. *Physical Review B* **88**.20 (2013): 205108.

[SI-14] Hansen, Daniel, and B. Sriram Shastry. Extremely correlated Fermi liquids: Self-consistent solution of the second-order theory. *Physical Review B* **87**.24 (2013): 245101.

[SI-15] Shastry, B. Sriram. Extremely Correlated Fermi Liquids. *Physical Review Letters* **107**.5 (2011): 056403.

[SI-16] Shastry, B. Sriram. Theory of extreme correlations using canonical Fermions and path integrals. *Annals of Physics* **343** (2014): 164-199.DOI:http://dx.doi.org/10.1016/j.aop.2014.02.005. (Erratum) *Ann. Phys.* **373**, 717-718 (2016). DOI:http://dx.doi.org/10.1016/j.aop.2016.08.015.

[SI-17] Gweon, G-H., B. S. Shastry, and G. D. Gu. Extremely Correlated Fermi-Liquid Description of Normal-State ARPES in Cuprates. *Physical Review Letters* **107**.5 (2011): 056404.

[SI-18] Shastry, B. Sriram, and Edward Perepelitsky. Low-energy physics of the t-J model in $d = \infty$ using extremely correlated Fermi liquid theory: Cutoff second-order equations. *Physical Review B* **94**.4 (2016): 045138.